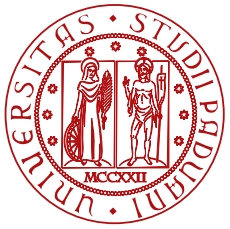

Università degli Studi di Padova

DEPARTMENT OF GEOSCIENCES

Tesi di laurea magistrale in Geophysics for Natural Risks and Resources

A Study of Upper Mantle Anisotropy in Cascadia Using Teleseismic Shear Wave Delays

Master Candidate

Matthew Hollinrake

Student ID 2070915

Supervisor

Prof. Manuele Faccenda

University of Padova

Co-supervisor

Dott. Brandon VanderBeek

University of Padova

Head of Department

Prof. Nicola Surian

University of Padova

Academic Year
2023/2024

The use of seismic tomography to characterise the upper mantle is a widely used technique. A common assumption within many of these models is one of an elastically isotropic mantle. It is widely accepted that simple shear deformation of anisotropic minerals (mainly olivine) present in the upper mantle creates a lattice preferred orientation (LPO). The formation of a LPO will create a seismically anisotropic upper mantle. When a linearly polarised shear wave (S-wave) encounters this anisotropy it splits into two orthogonal waves with one component aligned along the direction of greatest seismic velocity, typically the a-axis of olivine. Determining the direction of anisotropy from teleseismic S-wave arrivals can reveal information about strain conditions, mantle flow and other properties in the upper mantle. Accounting for anisotropy will lead to more accurate seismic tomography models whilst providing indications of convective flow, mineral fabrics within the upper mantle.

Mantle flow in the vicinity of the Cascadia subduction zone on the Pacific Northwest of the United States of America is highly complex and poorly understood. The Cascadia subduction zone is a relatively small yet complex geological system where a young (<10 million years old) Juan de Fuca plate is subducting beneath the North American plate less than 400km away from the mid ocean ridge where it is formed. Constraining the anisotropy in the upper mantle will provide insights into the interaction of mantle with the subduction zone and help understand the recent and future evolution of the geological system.

The Cascadia subduction zone has a dense network of permanent seismic stations as well as temporary deployments. Teleseismic S-wave data from 593 seismic stations for 411 earthquake events over a period of 4 years. The true travel time for each S-wave arrival was calculated using multichannel cross correlation, and delay time calculated with respect to AK135, a 1D earth reference model. The polarisation direction for each arrival was also calculated.

Two different inversions were completed, a deterministic iterative linearised inversion and a stochastic inversion using the Reversible Jump Markov Chain Monte Carlo method. For each, a tomographic model was produced with the relative S-wave velocity perturbation, and the 3D distribution anisotropic vector aligned to the symmetry axis of the hexagonal tensor (a good approximation for the a-axis alignment of olivine). This differs from previous studies which only discussed SKS splitting results, representing an average beneath the station.

The subducting Juan de Fuca plate is imaged as a high velocity anomaly with a North/South strike, and dipping Eastward at 60° below 100km depth. From the tomography model it does not appear to be continuous with a break in

the feature observed at 45°N. The presence of trench parallel anisotropy in the Southern sub-slab mantle, coupled with the rotational pattern observed to the South of the subducting slab are evidence for toroidal mantle flow from behind the slab round into the mantle wedge. The steep dip of the subducting slab imaged implies large amounts of steeping from the initial shallow subduction angle and slab rollback, which is a mechanism to cause toroidal flow.

Beneath the Juan de Fuca micro-plate, anisotropy under 200km deep is found to rotate from ridge perpendicular to trench perpendicular as the plate moves from ridge to trench. This implies that as the lithosphere cools and thickens away from the ridge, it shears the upper mantle, realigning the LPO to the motion of the plate. The Gorda micro-plate was found to have little to no influence on the anisotropic alignment beneath it. Instead it is proposed that the small deforming micro-plate simply accommodates shear between the larger Juan de Fuca and Pacific plates.

Contents

List of Figures

List of Tables

1

Introduction

Seismic body-wave tomography is a powerful tool, utilised widely to produce models of the earths interior. In regions such as the Cascadia subduction zone, located on the North West coast of the United States of America and Southern Canada, a dense network of seismic stations has allowed for high resolution imaging of the upper mantle (Obrebski et al., 2011). Commonly, these models are created assuming an isotropic earth, when it is understood that the earth is not an isotropic body. Common minerals found in the upper mantle, such as olivine, are known to be elastically anisotropic and orientate into lattice preferred orientations (LPO) due to strain under conditions found in the upper mantle (Karato, 2024). Where an LPO is formed in the upper mantle, we expect seismic anisotropy to be present. A linearly polarised shear wave (S-wave) encountering an LPO will split into two orthogonally polarised quasi s-waves, one component polarised in the plane of the highest seismic velocity (VanderBeek et al., 2023). This polarisation direction can be incorporated into seismic tomography models to reveal details about the orientation and distribution of anisotropy in the mantle.

There are two main reasons for including seismic anisotropy into the tomography models. Firstly, the anisotropy causes velocity variations that are dependent on the LPO fabric in the mantle, and with magnitudes comparable to those caused by changes in composition (VanderBeek et al., 2023). If not accounted for, this could lead to artifacts in the tomography models. Secondly, determining the magnitude and orientation of the seismic anisotropy allows us to link the seismic data to regional geodynamics. This can reveal information about deformational history, flow and other properties in the upper mantle. In

addition, accounting for anisotropy will lead to more accurate seismic tomography models whilst providing these indications.

Studies into seismic anisotropy have been undertaken using P, S and surface waves (Silver and Chan, 1991). However previous studies such as Zandt and Humphreys, 2008, Eakin et al., 2010, Becker et al., 2012, Bodmer et al., 2015 and Martin-Short et al., 2015, focused on one shear wave phase (SKS) and produced results displaying anisotropy per seismic station. Here the the variation of anisotropy with depth is not constrained.

This study uses teleseismic shear waves of multiple phases, collected over a period of 4 years. For each shear wave at each station, a two observables were calculated: the arrival time and the azimuth of polarisation of the incoming wave. We then utilised the iterative linearised inversion method of VanderBeek et al., 2023 to produce a tomographic model for the shear wave velocity, as well as the 3D distribution, orientation and magnitude of anisotropy present beneath the Cascadia subduction zone. We then use the tomography model and distribution of anisotropy to attempt to characterise the relationship between the geological history and present of the Cascadia subduction zone with mantle processes.

Alongside this, we undertake a Reversible Jump Markov Chain Monte Carlo (RJMCMC) inversion following the methodology of Piccolo et al., 2024. Seismic tomography is an under-determined problem, hence why most models use isotropic assumptions to minimise the unknowns, the linearised inversion processes must use regularisation to force uniqueness of solution (Piccolo et al., 2024). The choice of regularisation parameters ultimately has an effect on the model output. The use of RJMCMC should allow for the inversion to investigate multiple credible models without imposing uniqueness via regularisation (Piccolo et al., 2024). This method been shown to work for synthetic data, and we implement this for real seismic data here.

2

Geological Setting and Mantle Dynamics at Convergent Margins

Located in the Pacific North-West of the USA (figure 2.1), the Cascadia subduction zone is a relatively small yet complex system. Here the young oceanic lithosphere of the Juan de Fuca (JDF) plate system is subducting beneath the North American plate along a 1300km long trench located <100km off the coast (DiPietro, 2018).

The Cascadia convergent boundary is a small system, 400km in width from mid ocean ridge to trench at its greatest extent, containing a mid ocean ridge system, ocean trench and multiple transform and fracture zones. Recent evolution of the system over the last 60 Million years (Myr) has created the complicated picture seen in the present day.

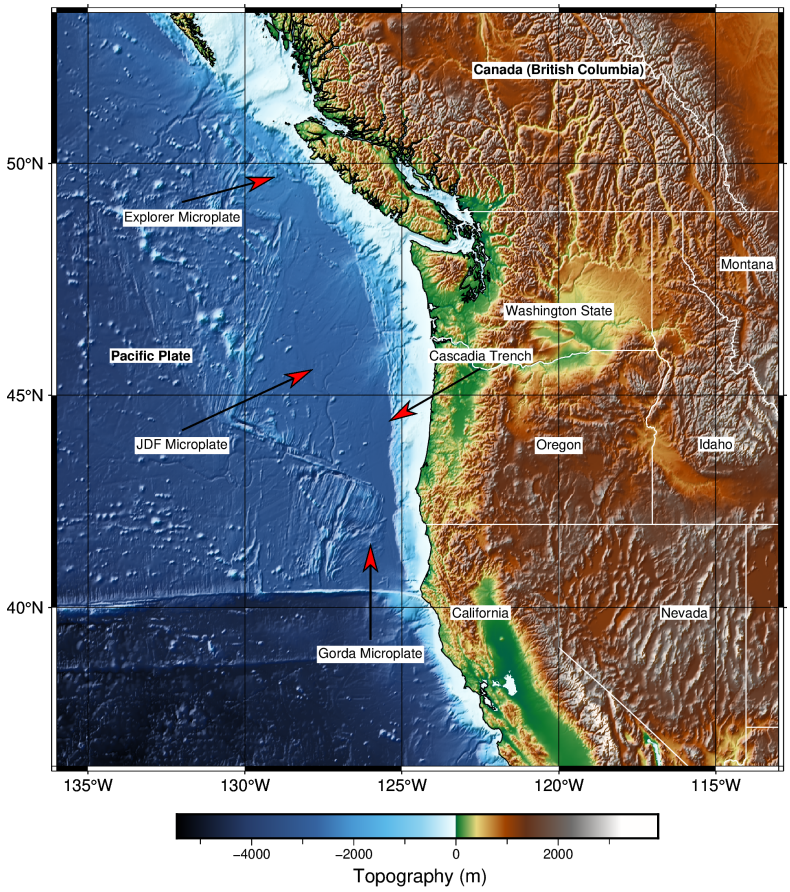

Figure 2.1: An overview of the Cascadia subduction zone located in the Pacific North-West of the United States of America. Thin white lines are the United States of America state boundaries and USA/Canada border. Major oceanic tectonic plate are annotated, to the West of the Cascadia trench the tectonic plate is the North American plate. Shading represents topography (onshore) and bathymetry (offshore). Topography data provided by the NASA STRM mission.

2.1 Tectonic History

In the Mesozoic Era (252 - 66 Myr) the JDF plate system did not yet exist. The predecessor to this plate system comprised of the Farallon plate, which was subducting along what would be the present day Western USA and Western South America. Approximately 80 Myr the Farallon plate was connected to the Pacific plate by a 10,000km spreading ridge (Rowan and Rowley, 2014), bound to the North by a triple junction with another extinct plate - the Kula plate, which broke off from the Farallon plate 83 Myr (Clennett et al., 2020). Subduction of the Farallon plate beneath the North American Plate has been occurring for 147 Myr (Clennett et al., 2020). Subduction of the Farallon plate was responsible for the Laramide Orogeny (70 - 40 Mry), which is the mountain building event that uplifted the Rocky Mountains found in central USA (English and Johnston, 2004). It has been proposed by (Bunge and Grand, 2000) that the Farallon plate subducted at a shallow angle, thus explaining the uplift so far from the location of the convergent margin. Subduction along the Western coast of the USA has continued until the present day.

Constraining the Mesozoic plate motions in the Pacific region is quite challenging as almost all plates of that age have been totally subducted. Plate motion reconstructions are undertaken using seafloor magnetic anomaly data (Seton et al., 2012), the accretion of terranes onto overriding plates (Clennett et al., 2020) and seismic tomography (Bunge and Grand, 2000) . The oldest magnetic anomalies associated with the Farallon plate are only 51 Myr (Rowan and Rowley, 2014) and are located off the coast of South America on the Nazca plate. The large Farallon plate is understood to have undergone five major breakups over the past 80 Myr, fragmenting into the Kula, Vancouver, JDF plates in North America, summarised in figure 2.2. To the south the Farallon plate broke up into the present day Cocos and Nazca plates (Seton et al., 2012). The Kula-Farallon spreading ridge subducted in its entirety beneath the North American plate, with a slab window evident in seismic tomography models that correspond to the subducted ridge system (Bunge and Grand, 2000). Consensus on the exact location of the ridge subduction remains unclear, possible locations range from Alaska to Northern Mexico (Fuston and Wu, 2020).

Between 47-49 Myr the Farallon plate was subject to more fragmentation creating the Vancouver Plate, along what is now known as the Murray Fracture Zone (Seton et al., 2012), with the Vancouver plate to the North and Farallon to the South. The cause of the plate breakup was possibly differential spreading

rates along the Farallon-Pacific ridge. This plate system continued to move eastward as spreading continued along ridges with the Pacific plate. At 30 Myr, the Murray fracture zone intercepts the North American plate creating the San Andreas Fault and the Vancouver plate becomes the JDF plate (Clennett et al., 2020).

Approximately 19 Myr, magnetic data shows a change in spreading rate and convergence rate for the JDF ridge and trench system (Wilson, 1988). The subducting JDF slab is seen to be discontinuous beneath Oregon at approximately 200km depth (Zandt and Humphreys, 2008), suggesting that the slab may have a hole or tear within it. It has been suggested that interaction with the Yellowstone mantle plume, which first occurred 17 Myr, may have triggered the up dip propagation of a tear (Obrebski et al., 2010). Whether the Yellowstone hot spot caused a tear in the subducted Farallon plate or not remains highly contested. Bunge and Grand, 2000's tomographic modelling images the old Farallon plate, as a seismic fast anomaly, beneath the Central and Eastern USA. Therefore if a deep mantle plume is the cause of Yellowstone's volcanism, it must have interacted with the plate at some point.

The continued breakup of the Farallon plate over the past 83 Myr created multiple slab windows as ocean ridge systems were subducted. These are regions in the upper mantle without a rigid lithosphere component which lead to episodes of trench retreat and slab rollback (Schellart et al., 2010). The steepness of the subducting plate has increased from the proposed shallow angle to the much steeper dip seen in modern tomographic images (Bunge and Grand, 2000). Figure 2.2 displays a model for the breakup of the plates, where in North America the initially very large Farallon plate eventually becomes the much smaller JDF plate system seen in the present day.

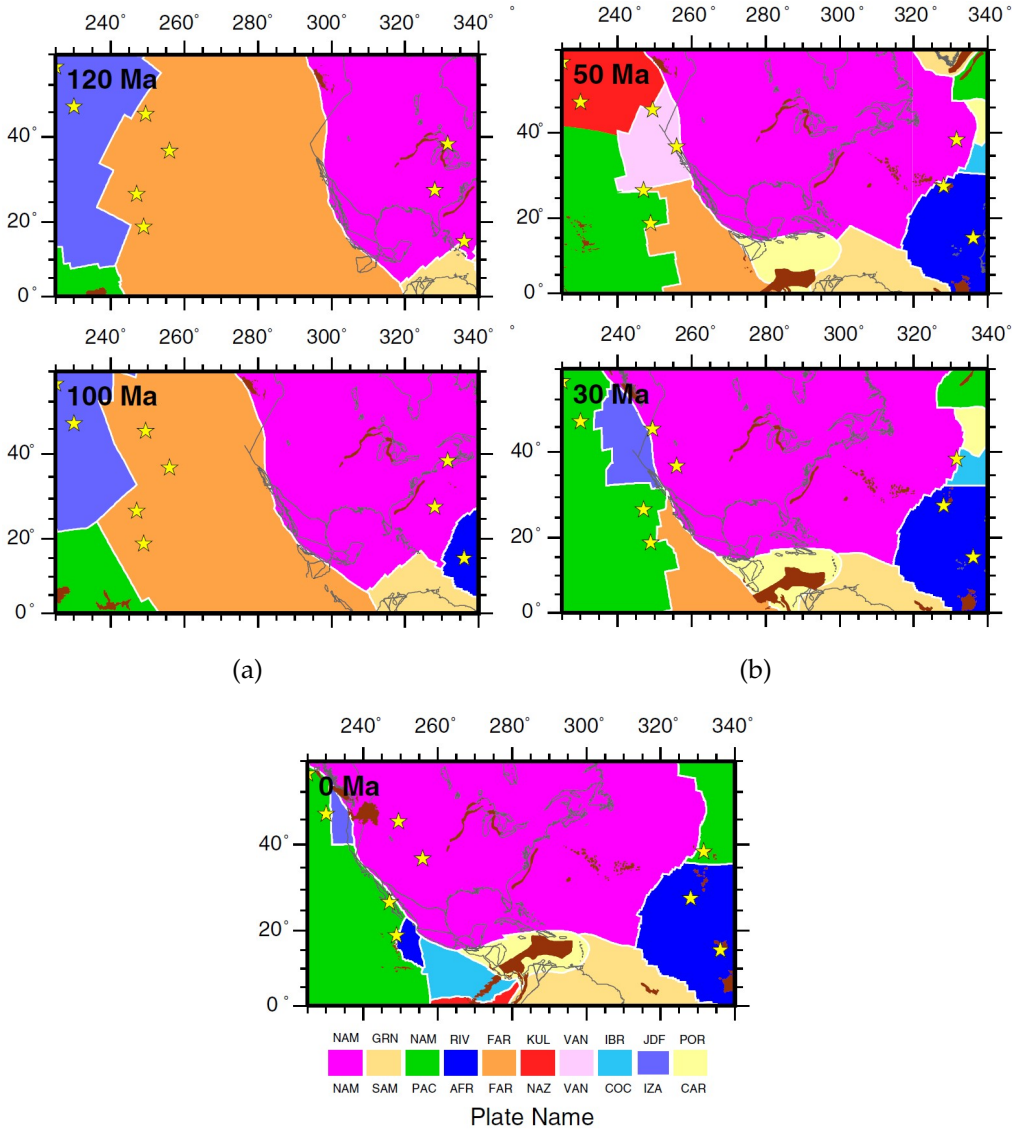

(a) (b)

(c)

Figure 2.2: Reconstruction of the Pacific North West plate motion for the last 120 Myr (Seton et al., 2012) Plates are indicated by colour: Purple - North American, Green - Pacific, Orange - Farallon, Red in figure (b) - Kula, elsewhere - Nazca, Light Pink - Vancouver, Blue in figure (a) - Izanagi, elsewhere - JDF, Light blue Cocos, Yellow - Caribbean. Yellow stars represent hotspot locations.

2.2 Present Day Setting

The present day setting off the coast of the Western USA comprises three separate micro-plates, from North to South they are the Explorer micro-plate, JDF micro-plate and the Gorda micro-plate which can be seen in figure 2.3. Each of the individual plates are separated from one and other by right lateral transform faults, and bound to the West by a spreading ridge with the Pacific plate. These three plates together will be referred to as the JDF plate system. The JDF plate system is subducting beneath the North American plate at the 1300km long Cascadia Trench, which runs from just North of Vancouver Island to just off the coast of Cape Mendocino in California. To the South, the system is separated from the Pacific plate by the Mendocino Fracture Zone (MFZ), another right lateral transform fault. A fault-fault-trench triple junction (MFZ - San Andreas Fault - Cascadia Trench) is formed at the meeting of the JDF, Pacific and North American plates. This triple junction is unstable and has been migrating northwards at a rate of 5 cm/yr (Sella et al., 2002) since its formation leaving behind a slab gap. A second triple junction is located off the coast of Vancouver Island to the North, a Ridge-Trench-Fault (Dellwood Knolls - Cascadia Trench - Queen Charlotte Fault). The triple junction was stable from 10 - 4 Myr but now is migrating northwards at 1-2 cm/yr (Riddihough et al., 1983).

Modern day rotation and fragmentation of the plate system is occurring due to along ridge spreading rate differences, 28 mm/yr to 60 mm/yr from the Gorda to JDF sections respectively (Martin-Short et al., 2015). The JDF plate's relative motion is approximately 50° North at 33 mm/yr and 43 mm/yr at the North and South respectively (Ismat et al., 2022). Subduction occurs obliquely at a rate of 12 mm/yr and at an angle of 60° North. The Cascadia trench is undergoing retreat of 24 mm/yr in a hotspot reference frame, caused by rollback of the subducting slab (Martin-Short et al., 2015) with the North American plate overriding the JDF plate system at a faster rate than subduction is occurring (Eakin et al., 2010).

The entire system is extremely narrow, at its widest extend the JDF ridge is only 400km from the Cascadia Trench. Therefore a young (under 10 Myr), warm JDF plate is being subducted (Han et al., 2016) making the Cascadia subduction zone a warm end member for global subduction zones. The age of subducted plate varies along trench strike, with the oldest subducted on the Southern part of the JDF micro-plate and decreasing in age Northwards. Due to the warm plate there is no Wadati-Benioff zone (Cheng et al., 2017) resulting

in tomographic modelling derived solely from teleseismic body waves. Seismic studies have found that before subduction the plate has a thickness <40 km, consistent with young oceanic lithosphere (Gao and Long, 2022). The young warm plate coupled with heavily sedimented outflow from rivers (DiPietro, 2018) and oblique convergence cause the very low rate of subduction of 12 mm/yr (Martin-Short et al., 2015). The length of the trench and short width of the plate means that the JDF plate system has the highest percentage of subduction of any system in the world, occurring along 43% of all boundaries (Schellart et al., 2010).

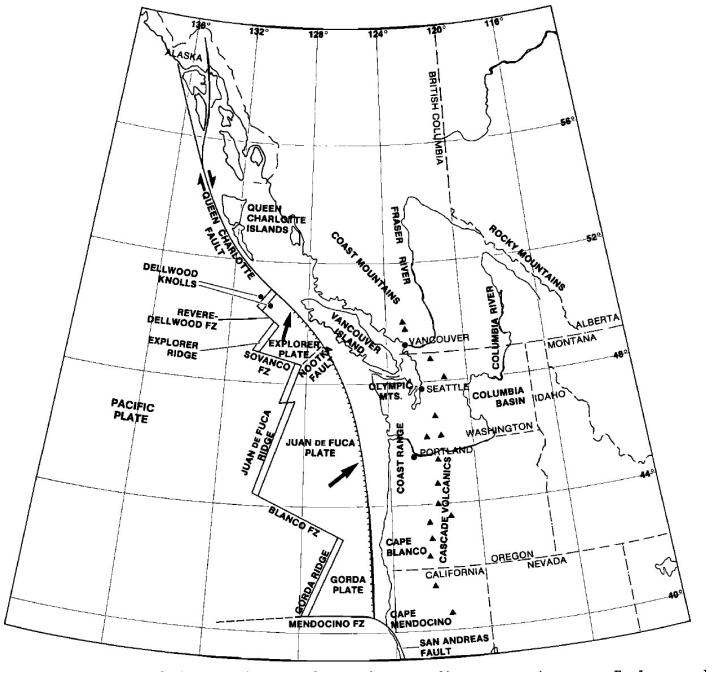

Figure 2.3: Overview of the JDF plate system Riddihough et al., 1983. Black arrows indicate plate motion. The Cascadia volcanoes are displayed as black triangles.

The Cascadia subduction zone system begins in the West along four spreading ridges with the Pacific plate displayed in figure 2.3, from North to South they are: Dellwood Knolls, Explorer Ridge, JDF Ridge, and the Gorda Ridge. From the Cascadia Trench to the Cascadia Volcanoes is the forearc portion of the system, with the volcanic chain running Mount Meager in British Columbia to Mount Lassen in Northern California (DiPietro, 2018). The continental back-arc region is characterised by thin lithosphere and extension seen in the Northern Basin and Ranges (Nevada, Southern Oregon, Southern Idaho and Western Utah), and Southern Canadian Cordillera (Oregon, Washington and British Columbia). The average lithosphere thickness for the Basin and Ranges area

is 60 - 70 km compared with 200 km thick on the North American Craton (Currie and Yu, 2023). Despite thin crust, both the Basin and Ranges and Southern Cordillera are high elevation features due to thermal isostasty, suggesting that local mantle upwelling and increased heat flow are present in this region (Hyndman and Currie, 2011). The formation of slab windows, slab rollback and a narrowing subducting slab all contributed to trench retreat which in-turn caused extension in the back arc 30 to 20 Myr (Schellart et al., 2010). However it is also argued that the extension in the Basin and Ranges was triggered by the beginning of the Yellowstone mantle plume but this is contested due to the lack of young plume associated volcanism (Zandt and Humphreys, 2008). Another proposed mechanism for the formation of the Basin and Ranges thin lithosphere is a process called lithospheric drip (Beall et al., 2017). This process is thought to be responsible for the initiation of extension following a period of shortening (Beall et al., 2017). The removal of dense eclogitised lower crust will cause uplift of the surface and crustal thinning (West et al., 2009). However it was formed, the Basin and ranges is known to have extremely thin crust (35km) compared to the North American craton.

2.3 Mantle Dynamics

Seismic anisotropy is an important property of the upper mantle that can be used to link the geodynamics of a region to the seismological data. The most important mineral in this process is olivine, which constitutes 50 - 80% of the upper mantle (Karato, 2024). Olivine is an elastically anisotropic mineral. Shear wave propagation along the fast [100] axis (figure 2.4) is ~18% faster than the slow axis [010] for a single crystal. (Long and Becker, 2010). The anisotropy is strongest in the upper mantle and decreases monotonically, with anisotropy of 2% at conditions of 11.8GPa and 1380°C which is analogous of 350km depth (Mainprice et al., 2005).

When deformation occurs at temperatures > 900°C (Currie et al., 2004), the olivine crystals align forming a lattice preferred orientation (LPO), which is thought to be the major influence on anisotropy. Most LPO's of olivine are formed by simple shear deformation where dislocation creep is the main form of deformation (Karato, 2024). The strength of anisotropy increases with increasing strain up to a strain of 100% to 150% (Karato et al., 2008), after which gran size reduction and phase mixing with pyroxene tend to weaken the fabric (Tasaka et al., 2017). Deeper into the mantle (>250km) anisotropy is less prevalent on

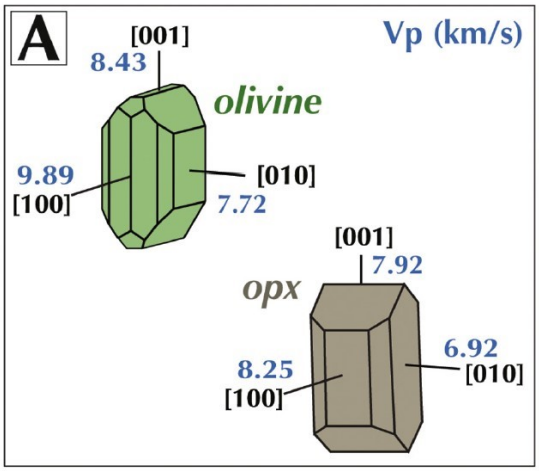

Figure 2.4: Crystallographic anisotropy of olivine and orthopyroxene crystals for P waves. The [100] axis is the referred to as the "fast axis" or a axis Bernard et al., 2021.

average due to either a smaller difference in slip system activities (i.e., less viscous anisotropy) or a higher efficiency of the diffusion creep mechanism (Warren et al., 2008), or the confinement of the deformation at shallow upper mantle depths. The latter is expected to occur in intra-oceanic settings, while at convergent margins intense deformation is well distributed over the entire slab depth range (e.g., Faccenda and Capitanio, 2021; 2013). The study of LPO fabrics is done in laboratories and data collected from exhumed mantle rocks. Studies on peridotie samples have found that the maximum concentration of a axis ([100]) alignment is along the direction of maximum shear (Long and Becker, 2010) allowing anisotropic studies to constrain information on shear conditions and mantle flow.

The anisotropy causes splitting of shear waves into two orthogonal waves. For most sampling directions the fast shear wave component will be polarized in the plane containing the a axis of the olivine, known as the fast axis (Warren et al., 2008). However four different olivine LPO fabrics exist and can be seen in figure 2.5. In simple shear types A, C and E all have the fast direction aligned to the mantle flow, whereas for B type, the fast axis is orthogonal to the flow. A type fabrics are the dominant fabric type in the asthenosphere. B type fabrics form in high stress, low temperature and with the presence of water (Long and Becker, 2010). For the Cascadia subduction zone, it is most likely that the A type fabric is present for most of the asthenosphere except for in the cold and wet corner of the mantle wedge were B type fabric may be present (Long and Becker, 2010).

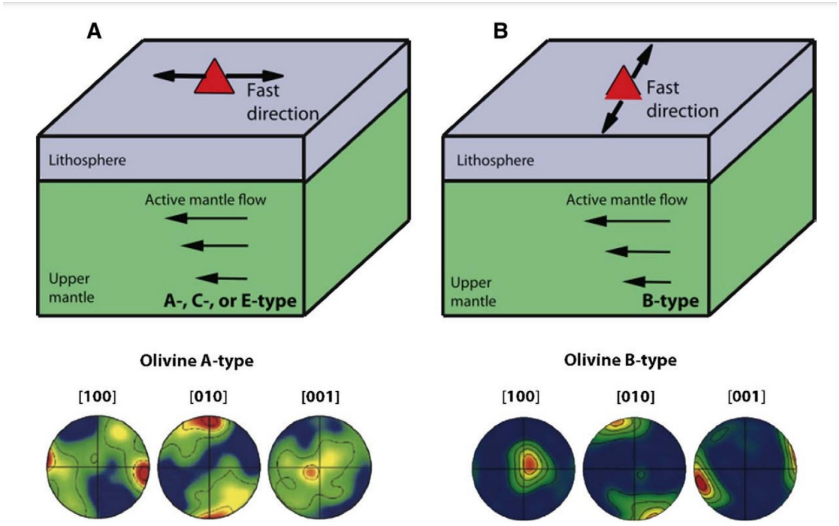

Figure 2.5: A summary of the 4 different Olivine LPO fabrics. For A, C, E type fabrics the [100] axis is aligned with the mantle flow. B type fabric has an orthogonal alignment to the mantle flow (Long and Becker, 2010).

As it has been demonstrated that grain-scale and rock-scale layering produce negligible elastic anisotropy in the mantle (Faccenda et al., 2019), and upper mantle LPO fabric is the dominant cause of shear wave anisotropy in seismic studies. The LPO indicates the most recent strain event or most dominant if there are multiple (Zandt and Humphreys, 2008). By identifying the anisotropy patterns, the behaviour of the viscous upper mantle flows can be inferred. Thus, by measuring and interpreting seismic anisotropy patterns may help in deciphering the relatively complex picture of the Cascadia subduction zone where the upper mantle conditions relatively unknown as a result of the multiple plate break up events.

Currently there are two end member models for mantle flow regimes at a subduction zone (figure 2.6). One end member is the 2D entrained flow model where mantle flow is entrained to the movements of the plates, with corner flow present in the mantle wedge (Long, 2016). The type of mantle flow is confined in the vertical plane and is referred to as the poloidal component. The other end member model is three dimensional. Here toroidal flow establish in the horizontal (tangential) plane and the mantle flows from behind the slab around the side of the slab into the mantle wedge (Long, 2016). This is driven by overpressure caused by slap rollback, which is occurring in Cascadia. In numerical models for a narrow slab (300km half width) the retreating slab causes toroidal flow around its edge, which in turn causes sub slab extension parallel to the trench (Faccenda and Capitanio, 2013). In wider slab models, the entrained

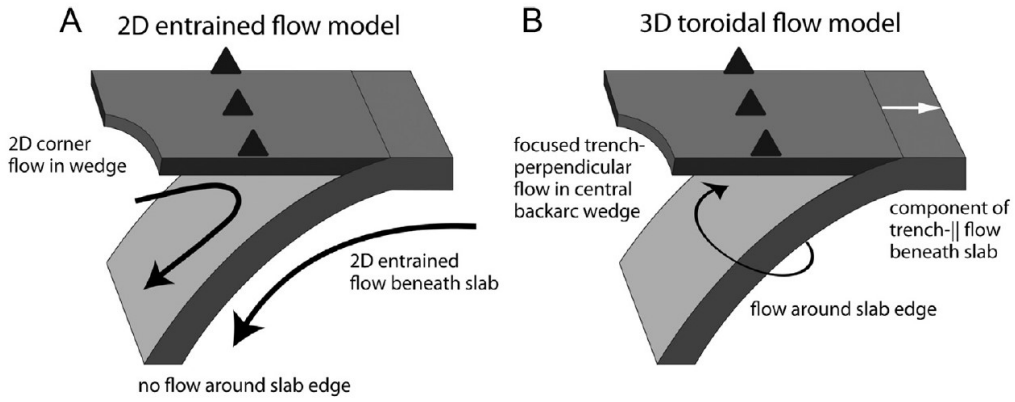

Figure 2.6: Diagrams of both the end member mantle flow models for a subduction zone. Figure A displays the 2D entrained mantle flow model. Figure B displays the 3D toroidal flow end member model (Long, 2016)

mantle above and below the lab display dip parallel alignment, also seen in the upper entrained mantle (Faccenda and Capitanio, 2013). The numerical models show that constraining the anisotropy is an important factor in constraining the geodynamic setting of a subduction zone. With the opening of slab windows occurring to both the North and South of the Cascadian subduction zone, and a relatively narrow slab undergoing rollback (Schellart et al., 2010) it is expected that some toroidal flow component should be present. As both these flow components constitute end member models for mantle flow, it is to be expected in the real world that a combination of the two is occurring.

3 Methodology

3.1 Data

Seismic data was collected for a period of over 4 years from between 25-07-2011 and 24-08-2015 (figure 3.1). 593 different seismic stations provided data from 25 different seismic networks (Table 7.1 appendix), with a combination of permanent and temporary station arrays, land based and ocean bottom seismographs. The area covered by seismic stations ranged from Vancouver Island to San Francisco from the North to South respectively, and from the JDF ocean ridge to Central Idaho from East to West respectively (figure 3.2).

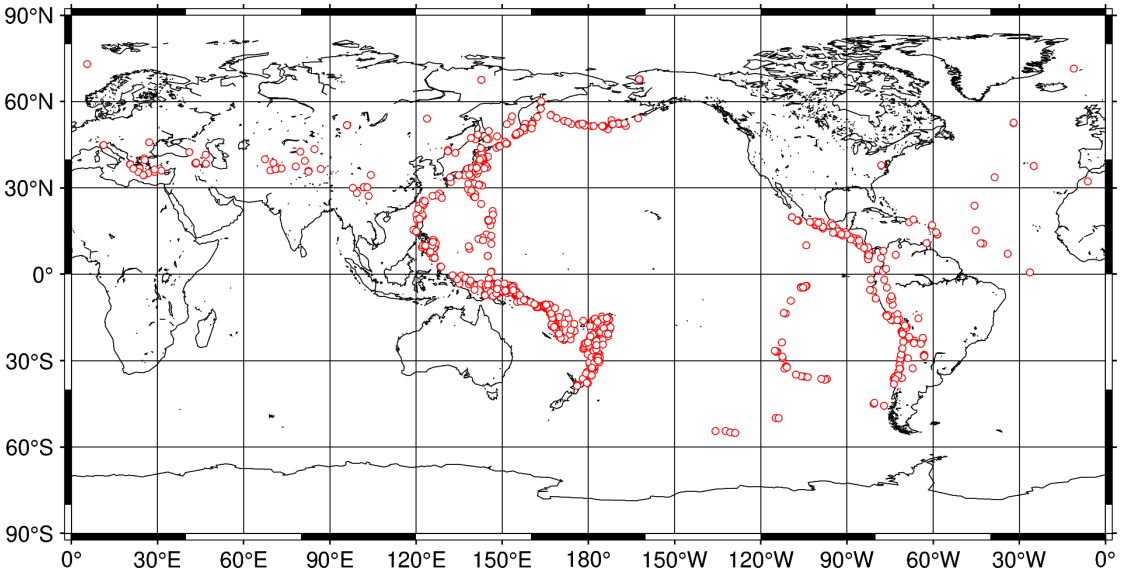

Figure 3.1: Epicentre location of the 411 earthquake events utilised in this study.

The earthquake data was selected to ensure that the arrivals within the

Cascadia region were of teleseismic waves, for which the source should be located at a distance of 30° from the receiver. Teleseismic waves have a near vertical ray-path through the upper mantle. 411 earthquake events were used, with the earthquake magnitudes from 5.7 M_w to 8.3 M_w. The study utilised data from four different S-wave phases: S, sS, Sdif and sSdif. The S phase is mantle shear wave phase that turns within the upper mantle, with larger offsets penetrating deeper (Storchak et al., 2003). sS is the same as S phase however the initial S-wave travels upwards and reflects off the free surface before traveling into the mantle (Storchak et al., 2003). Sdif refers to a shear-wave that has been diffracted along the core-mantle boundary (CMB), whilst sSdif is a combination of s-dif and sS. (Storchak et al., 2003).

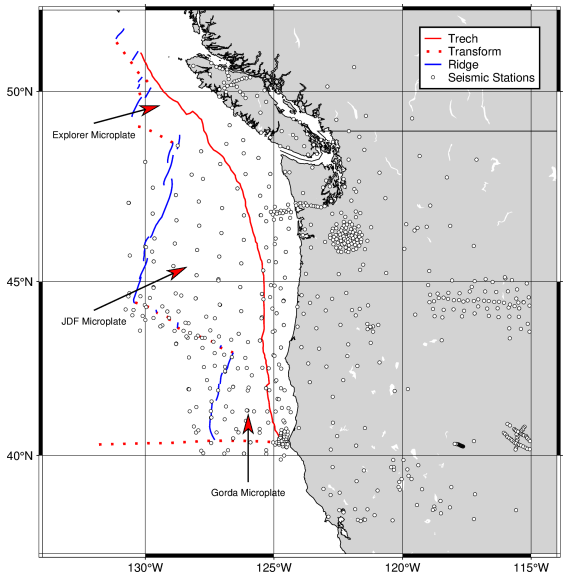

Figure 3.2: Locations of the seismic stations which were used in this study indicated as circles. Red line is the Cascadia trench, red dashed line are the transform faults, blue lines are mid ocean ridge sections and black lines are the coastline.

3.2 Theory and Derivations of Observables

When a linearly polarised S-wave enters an anisotropic region, for example a region with a strong LPO, it will split into two orthogonally polarised shear waves (figure 3.3). The two wave-forms (S_1, S_2) will propagate at different velocities resulting in two S-phases arriving at a seismic station. By calculating the polarisation azimuth of the incoming wave, and delay time between (S_1) and (S_2), it is possible to determine the azimuth and strength of anisotropy.

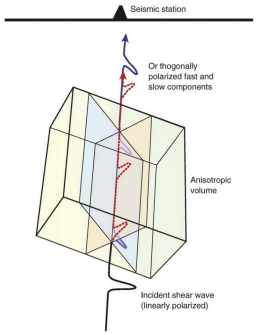

Figure 3.3: Diagram of an S-wave splitting when entering an anisotropic region (region with strong LPO) (Long and Becker, 2010). Incoming S-wave is linearly polarised and splits into a fast (blue) and slow (red) quasi S-wave. The blue plane represents the a-axis alignment of an Olivine LPO.

The propagation of seismic waves through a material is controlled by the elastic tensor, a 4^{th} rank elasticity tensor with 81 components (Itin, 2018). Due to symmetry, 21 components of this tensor are independent and can be represented by the symmetric 6x6 voigt matrix (Becker et al., 2006). This is too many independent components to be derived from seismic data as it would lead to underdetermined inverse problem. To reduce the number of free parameters, this study assumes hexagonally symmetry which, as discussed below, is a good approximation for most Earth materials (Becker et al., 2006).

By decomposing the olivine elastic tensor (the most significant anisotropic-forming mantle mineral) into different symmetry classes, Browaeys and Chevrot, 2004 demonstrated that the isotropic approximation accounts for 79.3% of the norm (magnitude) of the tensor, whilst the majority of the anisotropic component (15.2%) is hexagonal (figure 3.4). By assuming hexagonal anisotropy, the number of independent elastic coefficients reduces from 21 to 5 of which S-waves are primarily sensitive to 3 (Thomsen, 1986; Sieminski et al., 2007). Additionally, two angles are required to describe the azimuth and elevation of the hexagonal symmetry axis. For the purposes of seismic tomography, hexagonal

anisotropy can be represented as a vector describing the orientation and strength of anisotropy (VanderBeek et al., 2023). Since the upper mantle is known to comprise up to 80% olivine (Karato, 2024), the hexagonal approximation is a sound one.

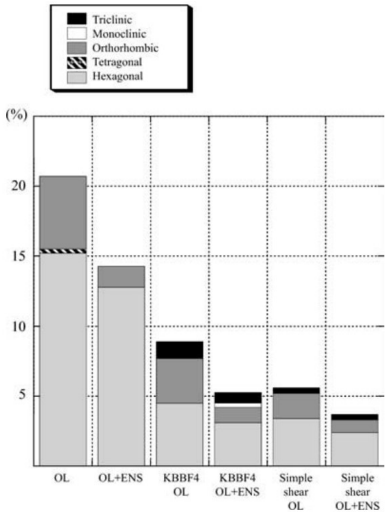

Figure 3.4: A graph displaying the decomposition of the anisotropic component of the elastic tensor for upper mantle minerals into different symmetry classes Browaeys and Chevrot, 2004.

The 6 by 6 representation of the 81 component elastic tensor matrix for a hexagonal symmetrical system is displayed below in equation 3.1 from Thomsen, 1986.

$$C = \begin{bmatrix} C_{11} & (C_{11} - 2C_{66}) & C_{13} & & & \\ & C_{11} & C_{13} & & & \\ & & C_{33} & & & \\ & & & C_{44} & & \\ & & & & C_{44} & \\ & & & & & C_{66} \end{bmatrix} \tag{3.1}$$

From this Thomsen, 1986 defined 5 parameters

$$\epsilon_{Thomsen} \equiv \frac{C_{11} - C_{33}}{2C_{33}} \tag{3.2}$$

$$\gamma_{Thomsen} \equiv \frac{C_{66} - C_{44}}{2C_{44}} \tag{3.3}$$

$$\delta_{Thomsen} \equiv \frac{1}{2C_{33}^2}[2(C_{13} + C_{44})^2 - (C_{33} - C_{44})(C_{11} + C_{33} - 2C_{44})] \tag{3.4}$$

$$\alpha_0 = \sqrt{\frac{C_{33}}{\rho}} \tag{3.5}$$

$$\beta_0 = \sqrt{\frac{C_{44}}{\rho}} \tag{3.6}$$

These 5 "Thomsen parameters" can be used to write equations for two shear waves velocities, v_1 and v_2, where v_1 is the phase velocity of the S-wave polarised in the plane containing the ray path and v_2 is the phase velocity of the S-wave polarised in the horizontal plane.

$$v_1(\theta) = \beta_0[1 + \frac{a_0^2}{b_0^2}(\epsilon - \delta)\sin^2\theta\cos^2\theta] \tag{3.7}$$

$$v_2(\theta) = \beta_0(1 + \gamma\sin^2\theta) \tag{3.8}$$

θ is the angle between the seismic ray path and the hexagonal symmetry axis. To reduce unknowns, VanderBeek et al., 2023 simplified equations 3.7 and 3.8 to

$$v_1 = \overline{v}_1[1 + f_1\cos 4\theta] \tag{3.9}$$

$$v_2 = \overline{v}_2[1 + f_2\cos 2\theta] \tag{3.10}$$

where $\overline{v}_1$ and $\overline{v}_2$ are the mean velocities. f_1 and f_2 are anisotropic fractions used to define the magnitude of the directional velocity variations of S_1 and S_2. Re-arranging and substituting we can use only v, f_1, f_2 to describe the anisotropy.

$$v_1 = \overline{v}\frac{(1 + f_2)}{(1 + f_1)}[1 + f_1\cos 4\theta] \tag{3.11}$$

We need to identify shear wave observables that can be related to the above anisotropic parameters. To do so, we follow VanderBeek et al., 2023. Consider a shear wave S that encounters an anisotropic LPO, it splits into the two quasi S-phases S_1 and S_2 in the fast and slow polarisation directions respectively. The quasi S-phases have different velocities through the anisotropic medium, so are

time shifted from one and other. Let the initial coordinate system be defined as $\hat{\mathbf{p}}$ - propagation direction of the incoming wave, $\hat{\mathbf{x}}$ - parallel to the polarisation direction, and $\hat{\mathbf{y}}$ perpendicular to both $\hat{\mathbf{p}}$ and $\hat{\mathbf{x}}$. From VanderBeek et al., 2023 the split shear wave can be described as

$$\mathbf{U}(\omega) = \mathbf{R}^{\mathbf{T}}\mathbf{\Gamma}\mathbf{R}U_0(\omega)\hat{\mathbf{x}} \tag{3.12}$$

Where U_0 is the incoming wave with an angular frequency of ω. $\mathbf{R}$ represents the rotational matrix which transforms the coordinate system from $\hat{\mathbf{x}}$,$\hat{\mathbf{y}}$ coordinate system into one aligned with the split shear waves S_1 and S_2.

$$\mathbf{R} = \begin{bmatrix} \cos(\psi - \xi) & \sin(\psi - \xi) \\ -\sin(\psi - \xi) & \cos(\psi - \xi) \end{bmatrix} \tag{3.13}$$

The angles in matrix $\mathbf{R}$, ψ and ϵ, are the azimuths of the hexagonal symmetry axis projected into the ray-normal plane and the initial linear S polarisation direction, respectively. $\mathbf{\Gamma}$ is the splitting operator, which assigns the relative delays accumulated due to the differing velocities to S_1 and S_2 as defined by Silver and Chan, 1991. Δt_1 is the delay time for S_1 and Δt_2 is the delay time for Δt_2

$$\mathbf{\Gamma} = \begin{bmatrix} \exp(-i\omega\Delta t_1) & 0 \\ 0 & \exp(-i\omega\Delta t_2) \end{bmatrix} \tag{3.14}$$

Equation 3.12 ignores phase shifts in the radial component when the wave interacts with the free surface (Silver and Chan, 1991), which is acceptable for steeply arriving teleseismic S-waves.

Following the method of VanderBeek et al., 2023, if $\Delta t_{1,2}$ are small when compared with ω, then a first order Taylor expansion of the exponential term in equation 3.14 is acceptable. In this data set, the mean magnitude of delay was 1 second, for S-waves with a period > 14 seconds. The split waveform equations can be written as

$$U_1(\omega) \approx (1 - i\omega[\Delta t_1 cos^2(\psi - \xi) + \Delta t_2 \sin^2(\psi - \xi)])U_0(\omega) \tag{3.15}$$

and

$$U_2(\omega) \approx \frac{1}{2}\sin(2(\psi - 2\xi))(\Delta t_2 - \Delta t_1)i\omega U_0(\omega) \tag{3.16}$$

From equation 3.15, the quasi shear wave U_1 is approximately the original waveform U_0 with the delay applied of the magnitude

$$\Delta t = \Delta t_2 + (\Delta t_1 - \Delta t_2)\cos^2(\psi - \xi) \tag{3.17}$$

and for equation 3.16 the quasi shear wave U_2 is the time derivative of the original waveform scaled by the splitting intensity described in Chevrot, 2000, and defined below.

$$\Delta s = \frac{1}{2}(\Delta t_2 - \Delta t_1)\sin(2(\psi - \xi)) \tag{3.18}$$

The equations 3.17 and 3.18 are valid for a single anisotropic interval. They are known as the principal anisotropic delay and principal anisotropic splitting intensity (VanderBeek et al., 2023), called principal as this refers to the coordinate system they are calculated in, aligned to propagation and displacement. The total magnitude of Δt and Δs can be calculated by integrating along the entire path of the ray. For a path comprised of n individual parts of length dL, the along path integrals can be defined by VanderBeek et al., 2023 as

$$t = \sum_{i=1}^{n} dL_i[u2_i + (u1_i - u2_i)\cos^2(\psi_i - \xi_i)] \tag{3.19}$$

and

$$s = \frac{1}{2}\sum_{i=1}^{n} dL_i[u2_i - u1_i]\sin(2\psi_i - 2\xi_i)] \tag{3.20}$$

where $u1_i$ and $u2_i$ are the slowness of the the split shear wave S_1 and S_2 over the i^{th} interval of length dL_i. The slowness of the wave can be related to the elastic properties outlined in equations 3.10 and 3.11 (VanderBeek et al., 2023).

$$u_1 = u\frac{(1 + f_1)}{(1 + f_2)}[1 + f_1\cos(4\alpha)]^{-1} \tag{3.21}$$

$$u_2 = u[1 + f_2\cos(2\alpha)]^{-1} \tag{3.22}$$

u represents the mean slowness and α is analogous to θ in equation 3.11. When described by Thomsen, 1986, α was the phase angle with the symmetry axis. This can be assumed to be equivalent to the ray angle in the presence of weak anisotropy. The angle α is the dot product of the ray and the symmetry axis vectors (VanderBeek and Faccenda, 2021) such that, for an incoming ray of azimuth ϕ and elevation Θ, in a hexagonal symmetrical medium with symmetry axis of azimuth Ψ and elevation γ,

$$\cos(\alpha) = [\cos(\phi - \Psi)\cos(\Theta)\cos(\gamma) + \sin(\Theta)\sin(\gamma)] \tag{3.23}$$

From VanderBeek et al., 2023, the polarisation angle of S_1 (ψ), is parallel to the hexagonal symmetry axis in the plane of $\hat{\mathbf{x}}$, $\hat{\mathbf{y}}$ plane. VanderBeek et al., 2023 defines

$$\psi - \xi = \arctan\left[\frac{-\sin(\phi - \Psi)\cos(\gamma)}{\cos(\phi - \Psi)\sin(\Theta)\cos(\gamma) - \cos(\Theta)\sin(\gamma)}\right] - \xi \tag{3.24}$$

The main benefit of this method by VanderBeek et al., 2023 is that the arbitrarily orientated anisotropy can be described with only 5 parameters (u, f_1, f_2, Ψ, γ), and geometric parameters to describe the path of the ray (dL, ϕ, Θ). The above equations are used to calculate the observables, the following section discusses how the observables are measured for the earthquake data.

3.3 Measuring Azimuth and Delay

To determine the true travel time and polarisation direction, the S-wave arrival times and azimuth of polarisation for each S-wave arrival for each earthquake event were calculated. The travel time must be calculated in the direction of polarisation (VanderBeek et al., 2023). For each event the earthquake data for the relevant receivers, was bandpass filtered between and 12s and 33s. Three component stations were used in this analysis. To measure delay times, the wave-forms are first rotated into the transverse, radial, Z coordinate system (TRZ) where the radial component lies along the back azimuth. The wave-forms are aligned initially with reference to a 1D earth model - AK135 (Kennett et al., 1995). Because the initial polarisation of the incoming shear wavefield is unknown, it is estimated from the stack of all 3-component S-waves recorded for a single event in the TRZ coordinate system (VanderBeek et al., 2023; thick black line figure 3.5a).

To align the traces, an initial iterative multi-channel cross correlation (MCC) is applied with a window length of 20s. Then a second MCC is performed with a narrowed window length of 10 seconds. For both the MCC steps the arrival time of the stacked trace is combined with the relative delay of each individual trace to obtain an arrival time value on the transverse channel.

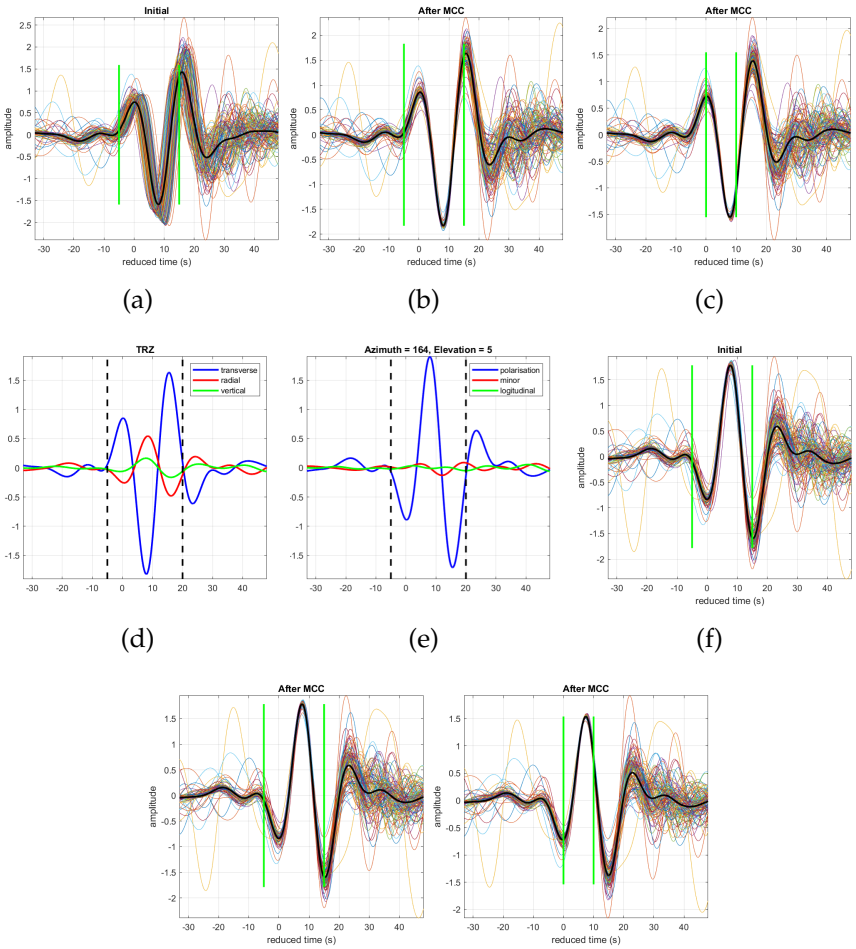

Figure 3.5: A summary of the steps undertaken during the MCC analysis of the S-waves. (a) The data is aligned on the transverse channel using the AK135 reference model as a guide. The vertical green lines represent the MCC window, coloured traces are the data and thick black trace is the stacked waveform. (b) The aligned wave forms after the first round of MCC with a window length of 20s. (c) The aligned wave forms after the second round of MCC with a window length of 10s. (d) Stacked data for all three of the channels in the transverse-radial-z coordinate system. (e) Stacked data for all three channels after rotation into the principle coordinate system. Polarisation line denotes the channel with the largest eigenvalue, azimuth and elevation angles for the quasi S-wave. Longitudinal channel points along the ray path, and minor is perpendicular to both. (f) Wave forms on the polarisation channel. (g) First MCC of the polarised channel with a 20 second window. (h) Second MCC of the polarised channel with a window of 10 seconds.

Once the updated arrival times were computed, polarisation analysis was undertaken. Firstly the covariance between the demeaned components was calculated, with he largest magnitude eigenvalue denoting the principle polarisation, the eigenvectors are used to calculate the azimuth and elevation angle of the incoming shear wavefield (VanderBeek et al., 2023). The second rotation of the seismogram is into the principle coordinate system, with one component aligned with the principle polarisation azimuth. MCC with first 20s then 10s window is then applied as above to obtain the arrival times for the polarised wave.

The updated travel times were corrected to account for shallow crustal structure, as discussed in chapter 2, there is a large amount of sediment outflow from the rivers in Cascadia. Updated travel times were converted to delay times by subtracting travel time predictions from the the AK135 1D earth reference model (Kennett et al., 1995) using the TauP toolbox. TauP uses the method of Buland and Chapman, 1983 to compute ray path and travel time for any IASPEI recognised phase travelling through the earth (Crotwell et al., 1999). TauP calculates the travel time and distance of the ray using the following equations from Buland and Chapman, 1983.

$$T(p) = \oint \frac{u^2(z)}{q(p,z)} dz \tag{3.25}$$

$$X(p) = \oint \frac{p}{q(p,z)} dz \tag{3.26}$$

$$\tau(p) = T(p) - pX(p) \tag{3.27}$$

where p is the ray parameter, z is depth, and q is defined as

$$q(p,z) = (u^2(z) - p^2)^{\frac{1}{2}} \tag{3.28}$$

The delay time is simply the observed travel time - reference travel time, calculated with TauP using the AK135 reference model (Kennett et al., 1995). Demeaning the data per event was done to remove any source side effects, a large velocity perturbation near the source effecting delay times would in theory be present in all of the delay times of a single event..

3.4 Deterministic Inversion

A deterministic inversion was completed using the software Platform for Seismic Imaging (deterministic). The methodology for this inversion follows the methods outlined in VanderBeek and Faccenda, 2021 and VanderBeek et al., 2023. The aim of the inversion is to constrain the spacial distribution of the anisotropic parameters derived in section 3.2 from the observables we have retrieved in 3.3 (VanderBeek et al., 2023). It is necessary to have a linear relationship between the anisotropic parameters and the observed travel times (VanderBeek and Faccenda, 2021). The free parameters $(u, f_1, f_2, \Psi, \gamma)$ can be reduced as Becker et al., 2006 defined a linear relationship between f_1 and f_2. The anisotropic parameter values were assigned to realistic values for upper mantle rocks and are shown in table 3.1.

Thomsen Ratio	Value
$\frac{\epsilon}{f}$	-1.0
$\frac{\epsilon-\delta}{f}$	0.3101
$\frac{\gamma_t}{f}$	-0.6179

Table 3.1: Values chosen for Thomsen parameter ratios to use in the inversion.

The parameterisation of the model proposed by VanderBeek and Faccenda, 2021 was used, as unlike that proposed by Munzarová et al., 2018, this method allows for a starting isotropic model. VanderBeek and Faccenda, 2021 use the mean slowness $\overline{\mathbf{u}}$ and the three following anisotropic variables

$$A = |f_2| = \cos^2(\gamma)\cos(2\Psi) \tag{3.29}$$

$$B = |f_2| = \cos^2(\gamma)\sin(2\Psi) \tag{3.30}$$

$$C = \sqrt{|f_2|} = \sin(\gamma) \tag{3.31}$$

These four parameters are contained within the model perturbation vector (Faccenda and VanderBeek, 2023)

$$\Delta\mathbf{m} = |\Delta\overline{\mathbf{u}}, \Delta\mathbf{A}, \Delta\mathbf{B}, \Delta\mathbf{C}| \tag{3.32}$$

The discretisation of the model was on a regular grid with spacing of approximately 30km horizontally and 10km vertically, centred on the geographical coordinates of 123.0W and 45.0N. Half widths of the model were 9 degrees of longitude and 8 degrees of latitude, with the model depth of 700km and anisotropy

constrained to the upper 500km. A 1D isotropic velocity initial model was chosen, based on AK135 (Kennett et al., 1995) with a 9km extension applied to account for local topography. The inversion method used was iterative Gauss-Newton method to minimise a least squares objective function in the form of (Faccenda and VanderBeek, 2023, Aster et al., 2018)

$$\upsilon = \mathbf{res}(\mathbf{m}, \mathbf{\Delta m})\mathbf{C_d^{-1}}\mathbf{res}(\mathbf{m}, \mathbf{\Delta m}) + \epsilon\mathbf{\Delta m^T C_m^{-1}} + \lambda^2(\mathbf{Lm})^\mathbf{T}(\mathbf{L\Delta m}) \tag{3.33}$$

where $\mathbf{C_d}$ $\mathbf{C_m}$ are the data and model covariance matrices respectively. **res** is a vector containing data residuals, a non linear function of the the starting model and the model perturbations (Faccenda and VanderBeek, 2023). **L** is a Laplacian matrix to keep the model perturbations smooth, for this inversion the cumulative Laplacian was minimised with respect to the starting model (Faccenda and VanderBeek, 2023). λ and ϵ are scalars that control the spatial smoothness and norm of the model perturbation vector (Faccenda and VanderBeek, 2023) with 20 and 2 chosen respectively. λ and ϵ were the same for both anisotropic and isotropic parts of the inversion, such that each were equally weighted in the results. These values allow for spatially smooth result whilst not compromising the data fit. The linear system set up by the discretisation was solved using the least squares algorithm using QR factorisation (LSQR) outlined by Paige and Saunders, 1982.

The produced model is a 3D seismic tomography model containing v_s and an anisotropic vector aligned with the hexagonal symmetry axis. For interpretation, the results are displayed as velocity perturbation $d \ln v_s$ which is calculated by

$$d \ln v_s = \frac{v_{s(model)} - v_{s(ref)}}{v_{s(ref)}} \tag{3.34}$$

where $v_{s(ref)}$ is the reference velocity from the 1D velocity model AK135 (Kennett et al., 1995). Alongside the anisotropic inversion, an isotropic inversion was completed for the same dataset to compare results.

3.5 Stochastic Inversion

Along side the deterministic inversion, a second stochastic inversion was completed using the Reversible Jump Markov Chain Monte Carlo (RJMCMC) method, a Bayesian Monte Carlo solver (Piccolo et al., 2024). The inversion follows the methodology of Bodin and Sambridge, 2009 and was adapted to anisotropic seismic tomography by Piccolo et al., 2024. RJMCMC is an iterative stochastic approach where a sequence of models is produced in a chain, with each new model created from a perturbation of the previous model within a probability distribution controlled only by the current state of the model (posterior probability distribution) (Bodin and Sambridge, 2009).

The posterior probability distribution $p(\mathbf{m}|\mathbf{d}_{obs})$ is the probability density of the model parameters considering the data (Bodin and Sambridge, 2009). It is defined using Bayes' theorem as

$$p(\mathbf{m}|\mathbf{d}_{obs}) = \frac{p(\mathbf{d}_{obs}|\mathbf{m})p(\mathbf{m})}{p(\mathbf{d}_{obs})} \tag{3.35}$$

where $\mathbf{d}_{obs}$ is the vector defined by the observed data and $\mathbf{m}$ is the model parameter vector containing node coordinates and model values (Bodin and Sambridge, 2009). From Bayes' theorem, the data likelihood function and the prior distribution are used to calculate the posterior function (Wu et al., 2023). The likelihood function $p(\mathbf{d}_{obs}|\mathbf{m})$ is the the probability that given the current model $\mathbf{m}$, what is the probability of observing the data $\mathbf{d}_{obs}$ and is defined by Bodin and Sambridge, 2009 as

$$p(\mathbf{d}_{obs}|\mathbf{m}) \propto \exp \frac{-\phi(\mathbf{m})}{2} \tag{3.36}$$

where $\phi(\mathbf{m})$ is the objective or least-squares misfit function.

The model "nodes" are the nuclei of Voronoi cells each containing parameters of the model (Piccolo et al., 2024). For this inversion the model was parameterised as follows: x,y z location of the nuclei, $d \ln V_s$, f_s, Ψ and γ (the three spherical anisotropic parameters) where

$$d \ln V_s = \frac{\Delta v_s}{\overline{v_s}} \tag{3.37}$$

Δv_s is the velocity perturbation and $\overline{v_s}$ is the mean velocity. A 3D Voronoi diagram is constructed by using the nearest-neighbour interpolation scheme between the Voronoi nuclei (Piccolo et al., 2024). The values on the nuclei are

random variables in drawn from the prior distribution (Piccolo et al., 2024). For every iteration of the model in each chain (28 chains) the model is perturbed by a selected value. For this inversion the magnitude of perturbation was a Gaussian probability function with a standard deviation σ_d of 1% and within the range set for each of the parameter of the prior distribution. The ranges for each prior value are summarised in table 3.2.

Parameter	Initial Distribution	Range
$d \ln V_s$	uniform	$[-0.05, 0.05]$
f_s	uniform	$[0.00, 0.04]$
Ψ	uniform	$[-2\pi, 2\pi]$
γ	uniform	$[0, \pi/2]$

Table 3.2: Summary of prior values chosen for the the inversion

The model was run for $1{\cdot}10^6$ iterations, for each inversion, each parameter of the prior distribution is perturbed by a randomly chosen perturbations in the following list as defined by Piccolo et al., 2024:

1. A value of a parameter is perturbed by the Gaussian probability function.
2. The position of a nuclei is changed.
3. A new nucleus is created.
4. An existing nucleus is deleted.
5. The noise data is perturbed.

For each new model, acceptance or rejection of the new model is determined by the ratio of the new and old posteriors (Bodin and Sambridge, 2009). The initial model contained 100 uniformly distributed nuclei and was isotropic with uniform initial distribution of the parameters, with anisotropy limited to the upper 500km. The maximum number of nuclei is 10,000. 28 independent chains were run in parallel, each chain's results are interpolated to a fine grid, and averaged to produce a 3D tomographic model. The earlier iterations of the model were discarded, with the discarded sections known as the burn in period.

The stochastic inversions produce a 3D tomographic model with $d \ln V_s$, the anisotropic vector aligned with the hexagonal symmetry axis. An isotropic inversion was also run to compare results.

4 Results

4.1 Delay Times

At multiple stages of determining true travel times and polarisation azimuth for the S-waves, data were rejected for multiple reasons. As mentioned in section 3.1, a total of 411 earthquake events were initially selected. From this, 33 earthquakes did not contain discernible S-waves that could be used for delay time calculations, and were omitted from the dataset. Due to the location of the seismic stations with many along the coast and ocean bottom seismographs, noise was a large factor. Figure 4.1 displays an example of a two noisy traces (thick red lines) which failed to converge during the MCC. The amplitude of noise was often comparable to that of the arriving S-waves. These data along with any delays calculated to be greater than 8 seconds were also discarded, with 15 events containing at least one trace with such data. Of 411 earthquake events, 378 were found to contain sufficient data quality as to be included in the modelling process.

As discussed in section 3.3, the data was demeaned per event with the aim to remove any source side effects on delay times relative to the AK135 reference model (Kennett et al., 1995). The standard deviation (σ_{delay}) of the delays was 1.34 seconds. Any delays that were $\pm 4\sigma_{delay}$ were rejected. From 41777 observations, 512 were rejected. The mean magnitude of delay was 1.01 seconds.

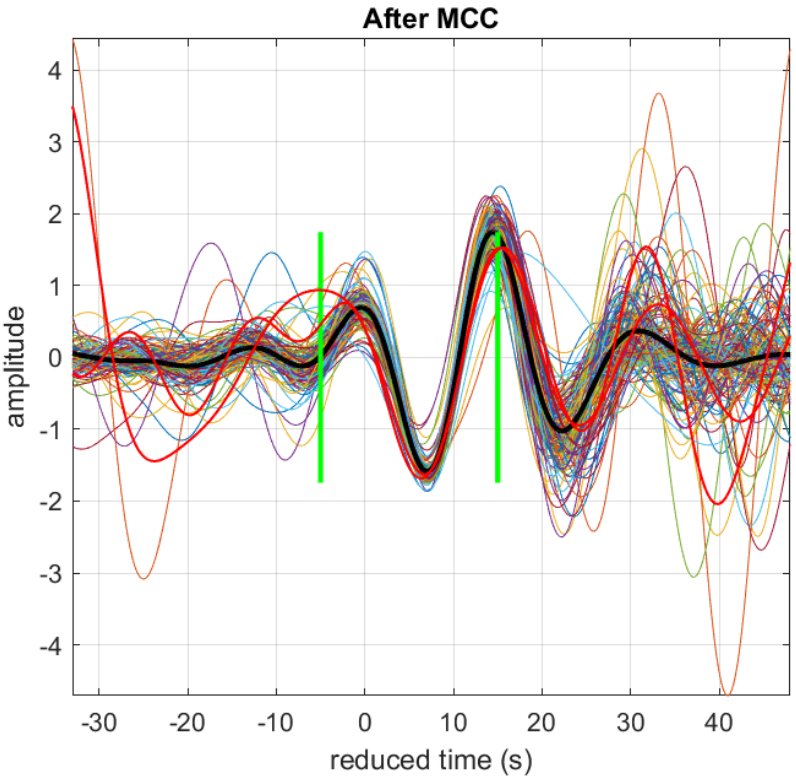

Figure 4.1: An example of a noisy seismic trace which failed to converge during MCC. Thick red lines indicates the failed traces which were removed from the data, thick black line is the stacked traces, all other lines are individual traces.

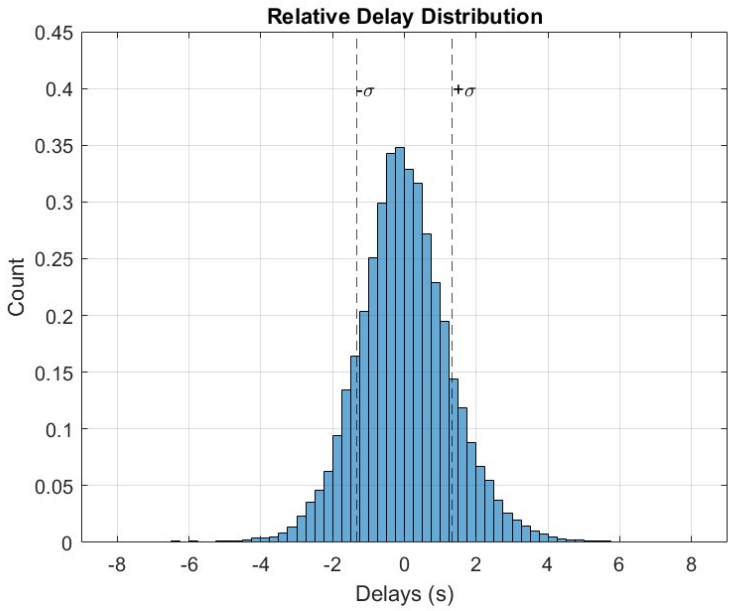

Figure 4.2: Histogram displaying the distribution of demeaned delay times. Vertical dashed lines are ± the standard deviation for the entire dataset.

For initial observations, the mean delay at each station can be plotted. A positive mean delay corresponds to arrivals later than that predicted by AK135 (Kennett et al., 1995), therefore a slower travelling S-wave and vice versa. The west, along the JDF and Gorda ridge sections of the JDF plate are characterised by positive mean delays (figure 4.3), with delays from 0.25 seconds up to the maximum delays seen in the data (<3 seconds). A contrast between the JDF micro-plate and Gorda micro-plate is observed, the JDF micro-plate has negative delays whereas the Gorda micro-plate was consistently positive delays. Along the location of the Cascadia volcanic chain, running North/South along approximately 122°W, a linear trend of negative delay times can be observed, with greater magnitude in the North. The back-arc region (120°W and Eastward) has two distinct regions. From 43° to 44° the mean delay times change from positive to the South, to mostly negative to the North.

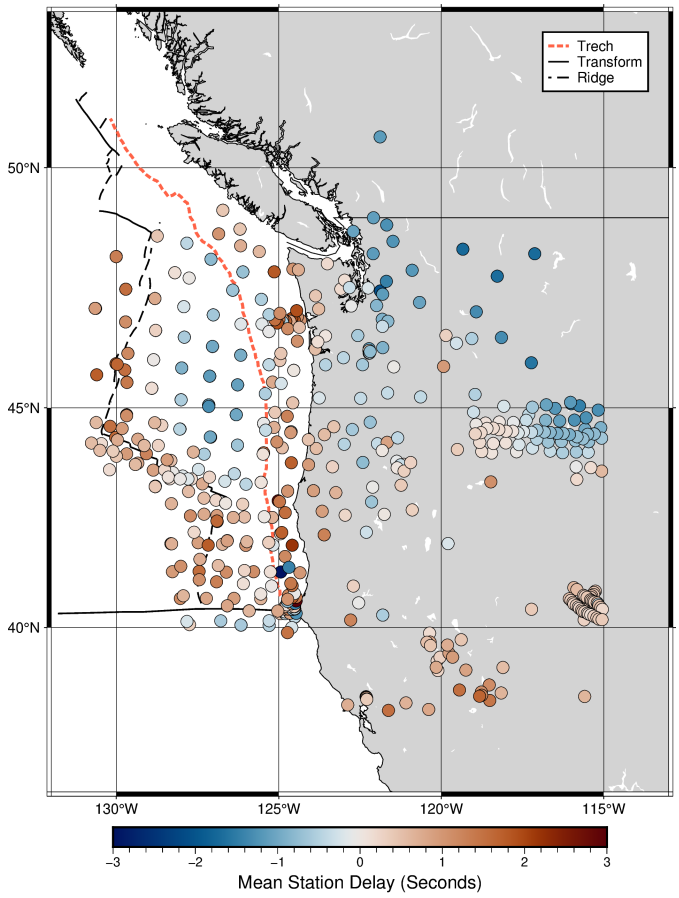

Figure 4.3: Map of the survey area. Circles are individual stations, fill is the mean delay time recorded at that station for all earthquake events. Red dashed line is the Cascadia trench, solid black lines are transform faults and dashed black lines are mid ocean ridge sections.

4.2 Deterministic Inversion

4.2.1 Inversion and confidence

The deterministic inversion was run until the sum of squared residuals compared with the previous iteration do not drop by a statistically significant amount, by using a F-test with a 95% confidence rate (VanderBeek et al., 2023). Convergence for this dataset was achieved in four iterations. Figure 4.4 contains data coverage plots for the inversion for slowness (Δu). The plots are derived from the squared weight derivative sum of the Jacobian elements from the inversion. It can be observed that at shallower depths, the higher coverage map roughly matches station coverage in figure 4.3, better coverage aligning with station density. With increasing depth, the region of coverage is greater, which is to be expected with teleseismic waves arriving at steep angles. The model overall has very good data coverage and can be interpreted with confidence.

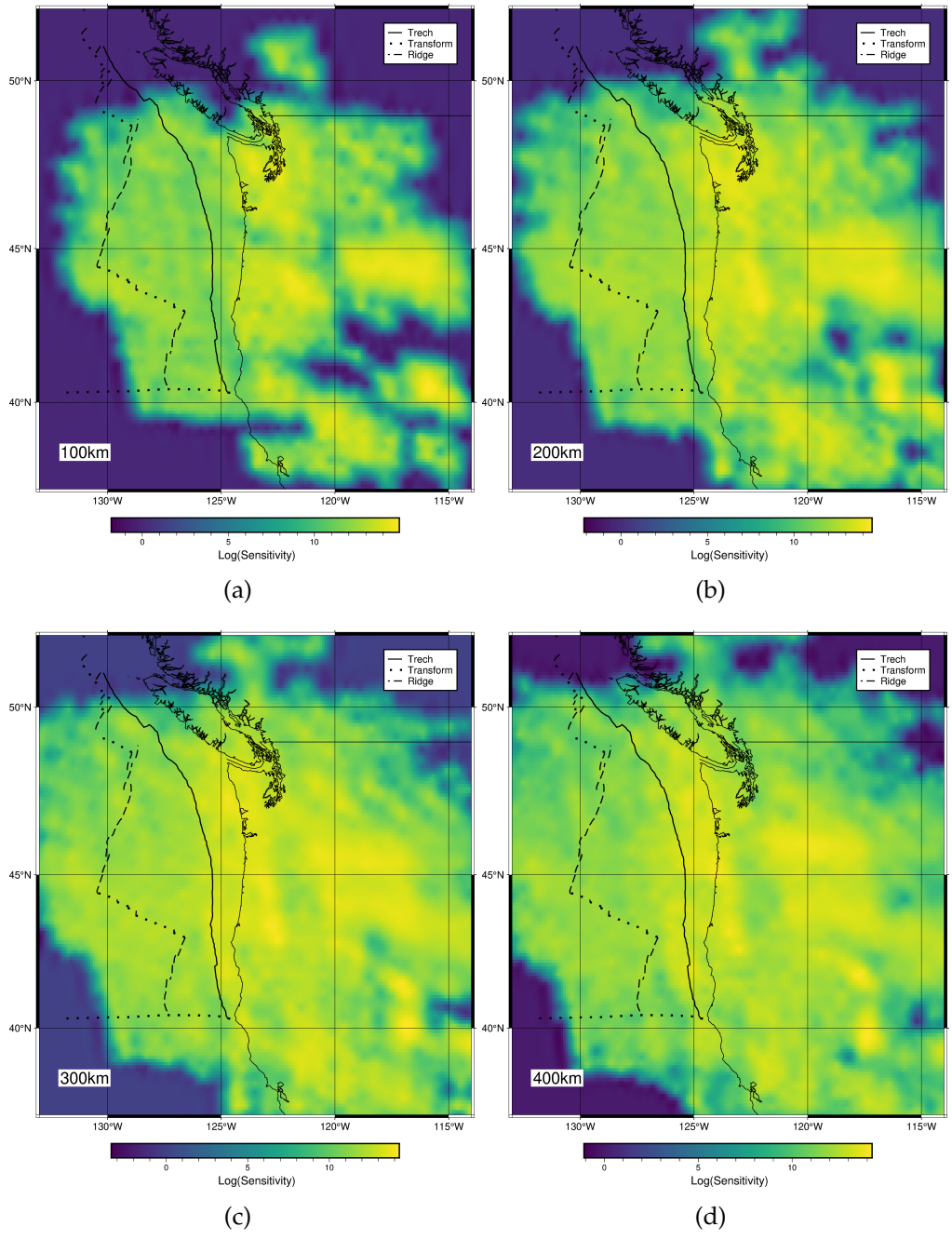

Figure 4.4: Logarithmic sensitivity plots for the deterministic inversion results. Depth of each slice is displayed in the bottom left corner of each image. Thin black line is the Pacific coastline of the USA and Canada, other lines are tectonic features indicated by legend in top right corner.

4.2.2 Inversion Results

The results of the inversion are presented as horizontal slices of the 3D tomography model with the velocity perturbation ($d \ln v_s$) which is the ratio of the modelled velocity with reference to the AK135 velocity model (Kennett et al., 1995) $\frac{(v_s - v_{sref})}{v_{sref}}$. The anisotropic vector, aligned to the hexagonal symmetry axis, is displayed as quivers and scaled to the magnitude of anisotropy. The results are displayed in figure 4.5. The shallowest part of the model is not interpreted, due to a lack of resolution from teleseismic shear waves. In the shallowest part of the mantle and crust, the incoming waves do not cross each other and therefore resolution is lower (Obrebski et al., 2011).

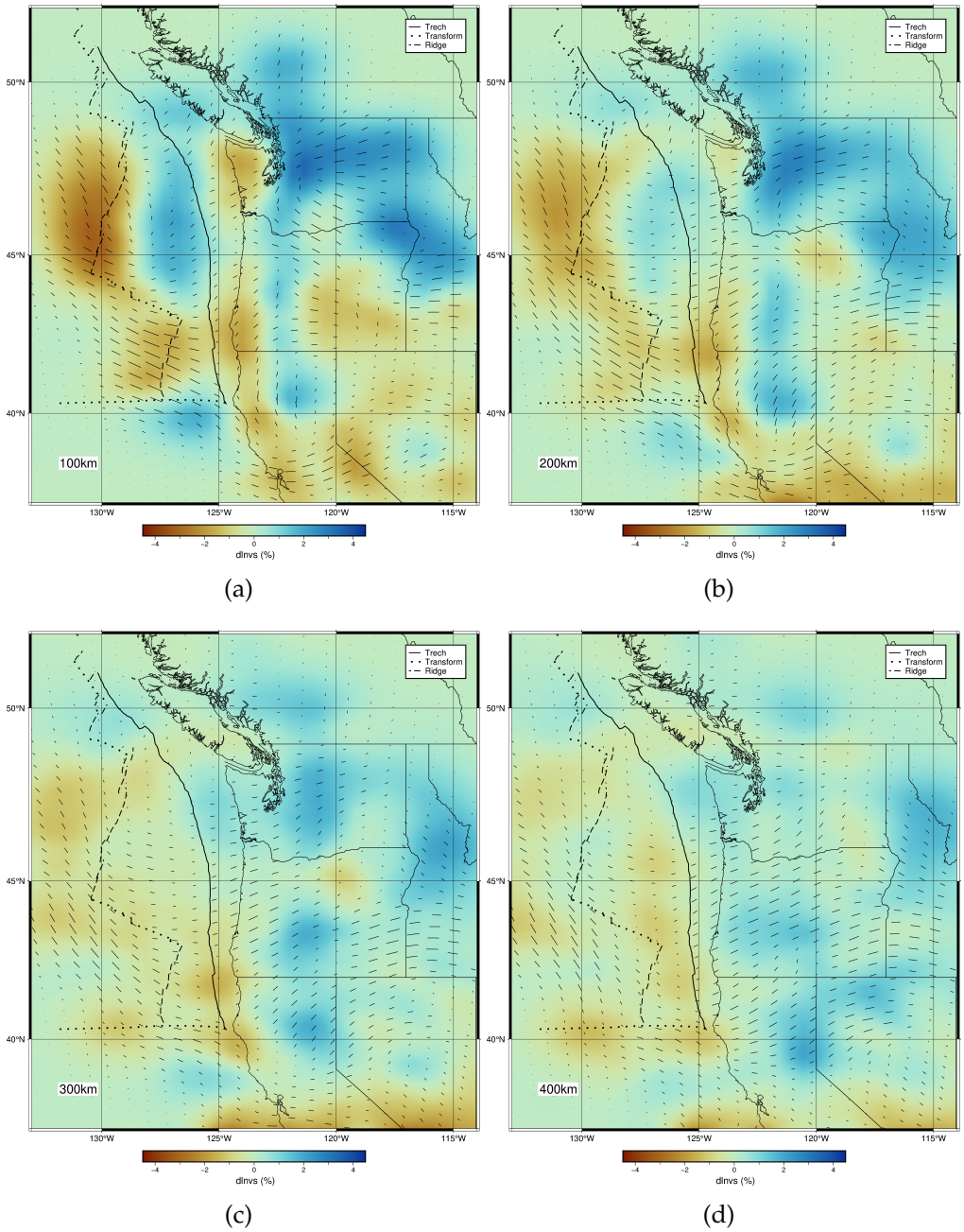

Figure 4.5: Horizontal slices of the Deterministic inversions with results displayed at 4 depth intervals: (a) 100km, (b) 200km, (c) 300km, and (d) 400km depth. Thin black lines are the USA and Canadian coastline, and USA state boundaries. Colour-scale represents velocity perturbation with reference to AK135 velocity model (Kennett et al., 1995). Hexagonal symmetry axis are plotted as quivers and scaled to magnitude. Thick black lines are offshore tectonic boundaries corresponding to the key in the top right corner.

The general trend is one of decreasing heterogeneity with depth. The greatest velocity anomalies are located within the upper 300km of the model with perturbations of ±4.5%. The areas located on the boundary of the model show zero velocity anomalies which is to be expected when compared with the coverage map shown in figure 4.4.

Along the JDF ridge and Gorda Ridge, the model is characterised by low velocity anomalies, -4.5% and -2.0% respectively. These areas are most prominent at shallower depths with the amplitude decreasing with depth. For the JDF micro-plate, a low velocity anomaly at the ridge then becomes a high velocity anomaly in the upper 200km between the ridge and fore-arc. This is not seen with the Gorda micro-plate which has a continuous low velocity anomaly to 400km beneath the ridge and plate.

In the upper 200km, a prominent continuous, North/South striking high velocity anomaly can be observed, which runs from the Mendocino triple junction in the South, to the Southern tip of Vancouver Island in the North at approximately 122°W at 100km depth. With an amplitude between 2.5% and 4.5%, this is inferred to be the subducting JDF plate. It is observed to be steeply dipping to the east (60°), and is imaged deeper in the South (500km) than the North (300km). This anomaly is absent to the South of the Mendocino triple junction and is not continuous below 200km. The high velocity anomaly is extremely variable along strike and is not continuous below a depth of 200km. The along strike break in the feature is observed just south of the Oregon/Washington border at 45°N.

North and South regions the back-arc display a contrast of velocity anomalies, to the North of Central Oregon/Idaho is a fast anomaly to a depth of 300km, and slower to the South to a depth of 200km. The boundary between these anomalies occurs at 45°N in Oregon and 43°N in Idaho. The fast anomaly in the Northern back arc is imaged all the way to the base of the model at 48°N and is a prominent feature. In the South-East corner a consistent high velocity anomaly beneath central Nevada is observed, over 500km deep with 2% to 3% velocity perturbations.

The anisotropic vectors follow a similar general trend to the velocity anomalies where the magnitude decreases with depth. The most prominent trends occur in the upper 200km of the model.

Beneath the Gorda ridge, on both the Pacific plate and Gorda micro-plate side of the ridge, the anisotropic vector is ridge perpendicular. At depths greater than 200km the anisotropic vector beneath the Pacific plate begins to rotate from ridge

perpendicular to parallel to absolute plate motion (APM) of the Pacific Plate, whereas the Gorda plate remains relatively consistently ridge perpendicular. The dip of the anisotropic vector beneath the micro-plate is sub horizontal until the Cascadia trench. Here the dips rapidly increasingly trend to the East. This is not seen beneath the JDF micro-plate. At the North of the Gorda micro-plate once crossing the trench, the anisotropic vectors rotate counter clockwise to align North-East for Northern. The Southern portions of the plate (<42°N) show a more drastic approximately 75° rotation to almost North-South further inland from the trench.

South of the Mendocino fracture zone on the Pacific plate (39.5°N), the anisotropic vector is sub parallel to the APM. The direction of the anisotropic vector here is very consistent with depth.

The Southern end of the JDF ridge, South of 46°N, displays anisotropy perpendicular to the ridge, however moving North along the ridge this rotates to be sub parallel to the APM of the Pacific plate for shallower depths (< 150km). From 150km and deeper the anisotropic vector is sub parallel to the Pacific plate APM for all of the JDF ridge. Along the Southern most part of the JDF ridge and Blanco fracture zone (BFZ), the anisotropic vector is parallel to the strike of the BFZ, again in the shallower depths under 150km. Once again as depth increases past 150km, the anisotropic vectors on the Pacific plate side rotate to align with APM, whilst to the North the vectors rotate to align sub-parallel to subduction.

Moving from ridge to trench along the JDF micro-plate, the anisotropic vector rotates to be aligned North-East/South-West, more parallel to JDF/North American plate convergence direction. The transition between these two orientations occurs in a similar position to the transition from low velocity anomaly to high and is most prominent in the upper 2000km again. By the Cascadia trench, the anisotropic vector on the JDF micro-plate is parallel to sub parallel to APM. Beneath the central JDF ridge, the anisotropic vector is dipping vertically to sub-vertically. The Explorer micro-plate is not discussed due to lack of data coverage.

The anisotropic vector within 100km landward of the trench are fairly consistent with depth. Between the Cascadia trench and the Western coastline the anisotropic vector is sub-perpendicular to the trench. The exception here is the rotation of the vector previously discussed in the Gorda micro-plate.

In the upper 300km, at the Southern most extent of the low velocity feature identified as the subducting JDF slab, the anisotropic vector orientation appears to rotate around the edge of the slab. At latitudes similar to that of

the Mendocino triple junction, the anisotropic vector is oriented North-South in the fore-arc. To the South of the slab at approximately 38°N and in line with the slab, the vector is orientated roughly East/West. Moving towards the California-Nevada border, the anisotropic vector rotates to North-East/South-West. Beneath Southern Oregon, the anisotropic vector is again North-South oriented for depths shallower than 150km. This pattern of rotation becomes less evident with depth. At latitudes parallel to the break in the continuous "slab" feature (46°N), the anisotropic vector is sub-parallel to East-West. In the upper 200km the direction of the anisotropic vector rotates counter-clockwise southwards towards the edge of the feature, orientated North-South. This rotation is not visible below 200km. The anisotropic vector appears to diverge around the location of the break in the high velocity feature but at shallower depths than the break (<200km).

In the back-arc, in Northern Nevada, central Idaho, and North Eastern Washington, the shallow trend of the anisotropic vector is roughly parallel/sub-parallel to the APM of the North American plate with magnitude again decreasing with depth. There is evidence for a small rotation of the anisotropic vector to sub trench parallel in Northern Oregon. Within the vicinity of the down-going slab there are 3 groupings of North/South oriented anisotropic vectors. One located at its southern extent, the second at 44°N, and then from 49°N Northward. A region of N-S alignment is also observed in the upper 150km beneath southern Oregon in a region called the High Lava Plains (HLP), centred on 119°W and 44°N. For the Southern section of the slab, the anisotropic vectors with and immediately sub slap are dipping roughly parallel to the the subducting slab. The mantle wedge to the South show horizontal to slightly sub-horizontal dips towards the West.

4.3 Stochastic Inversion

4.3.1 Inversion and confidence

The RjMCMC inversion was run on 28 separate Markov chains, with the results of each chain combined to produce the final inversion results. Figure 4.7 displays how each of the chain evolved with iteration and the results from one single chain are displayed in 4.6. The inversion was run for $1 \cdot 10^6$ iterations and every 10^4 model produced was saved in a process called thinning. The burn in was chosen as 10 models meaning that the first 10 models were discarded and not included in the final results. From figure 4.7, it can be seen that the model varies greatly in the early iterations and these variations would create artifacts in the final model. Despite running for $1 \cdot 10^6$ iterations, the model has not yet converged, with the downward trends still clearly visible in figures 4.7 (a), (b), (d), and the number of cells still increasing in (c). Due to the extensive computational requirements to run the RJMCMC inversion, the decision was taken not to increase the number of iterations further for this work. To combine the models from each Markov chain (example in figure 4.6), each chain was interpolated to a fine grid and then merged to create a 3D tomographic model for $d \ln v_s$ and the anisotropic vector.

Unlike the data coverage map created during the deterministic inversion (figure 4.4), the RjMCMC inversion produces a map for statistically significant results denoted by the ratio of standard deviation and mean. Regions of the model coloured red (figure 4.8) have a ratio of 1 and should not be interpreted as there is no statistical support for the results in this region. The regions with the highest confidence are: Beneath the JDF and Gorda ridges, Gorda micro-plate, Washington state, Southern British Columbia, Idaho and along the Southern border of the model.

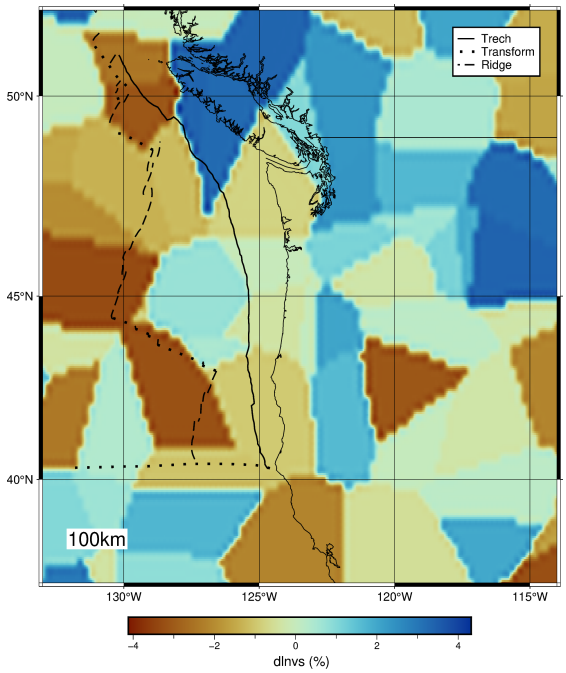

Figure 4.6: A Voronoi diagram, sliced at 100km created from one single giant Markov chain. The model is separated into cells and cell colour represents $d \ln v_s$.

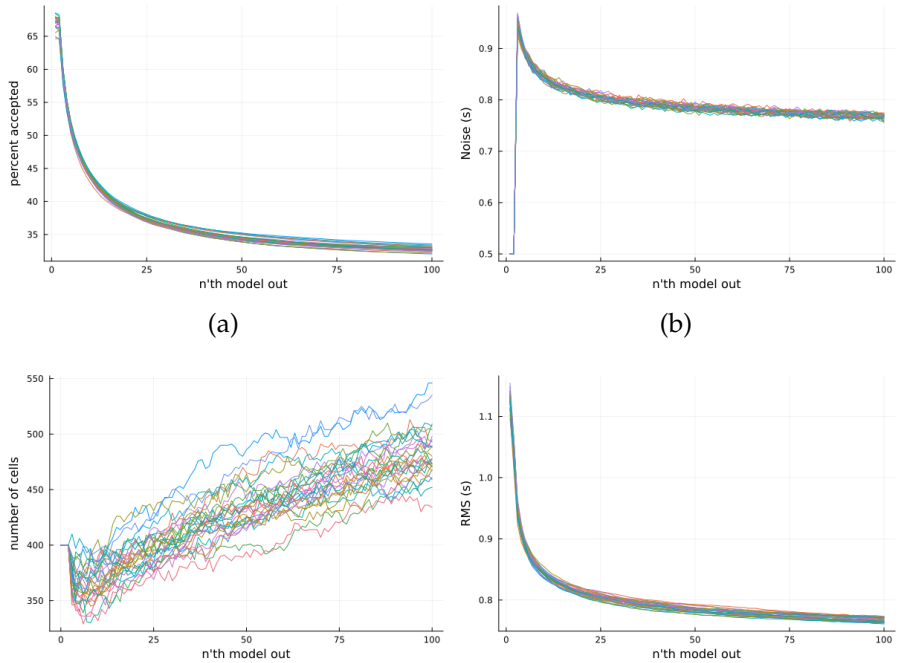

Figure 4.7: Figures displaying the evolution of the inversion with iterations. The x-axis represents the nth model produced. A model is produced ever 10^4 iterations, the x-axis totals $1{\cdot}10^6$ iterations. The individual graphs show coloured lines with one for each giant Markov chain and represent: (a) - The percentage of accepted models and each saving stage, (b) - The noise level at each saving stage, (c) - The number of Voronoi cells in each model at each saving stage, and (d) - The RMS of each model at each saving stage.

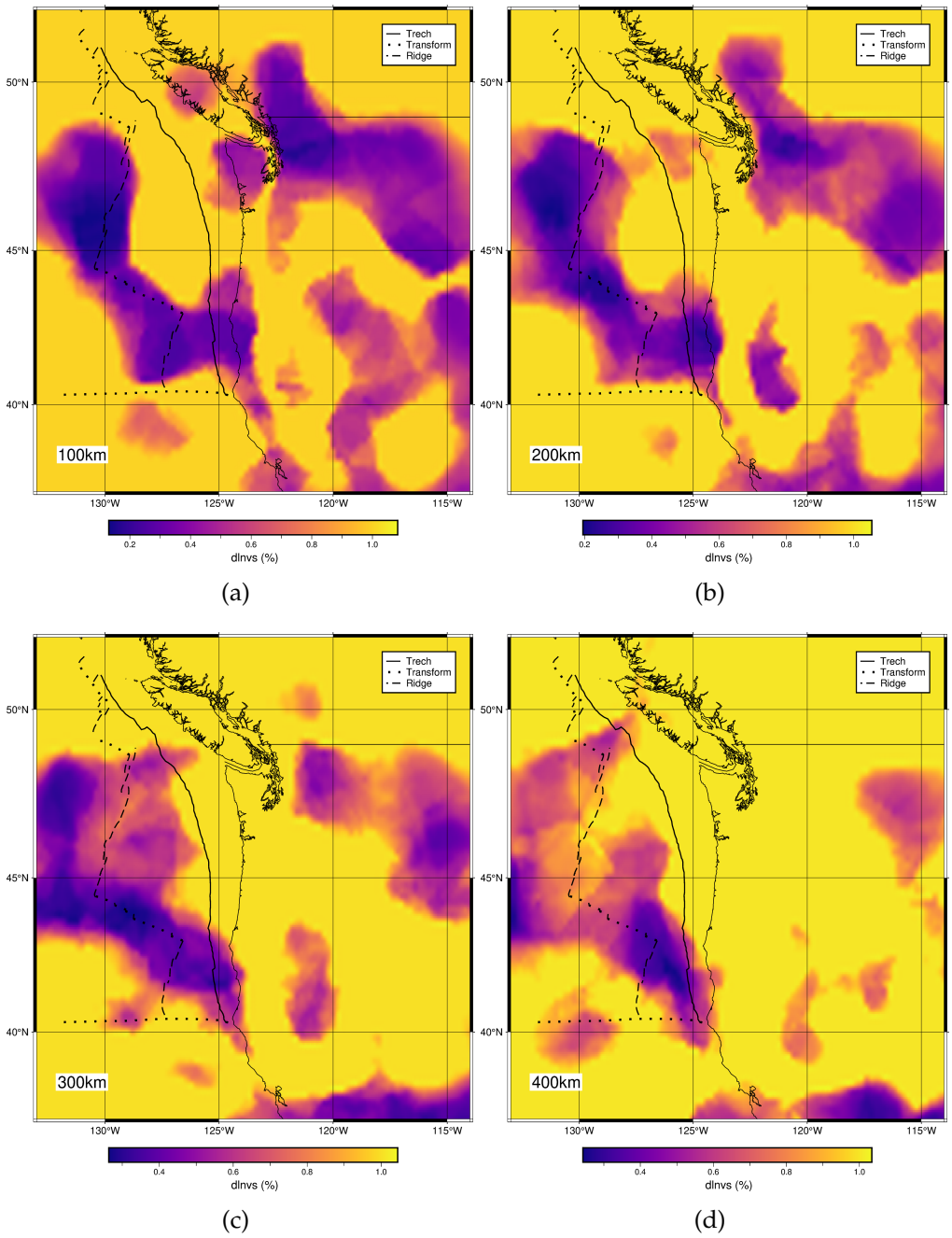

Figure 4.8: Standard deviation estimates for the velocity perturbations to mean V_S speeds. Higher uncertainties are represented by warmer colours.

4.3.2 Inversion Results

The inversion results are displayed as $d \ln v_s$ with the anisotropic vectors displayed as quivers and scaled to magnitude. From initial observations, the results of the RjMCMC inversion are remarkably similar to those obtained via the deterministic inversions. However it is only appropriate to interpret velocity anomalies and anisotropy from areas of the model with sufficient confidence.

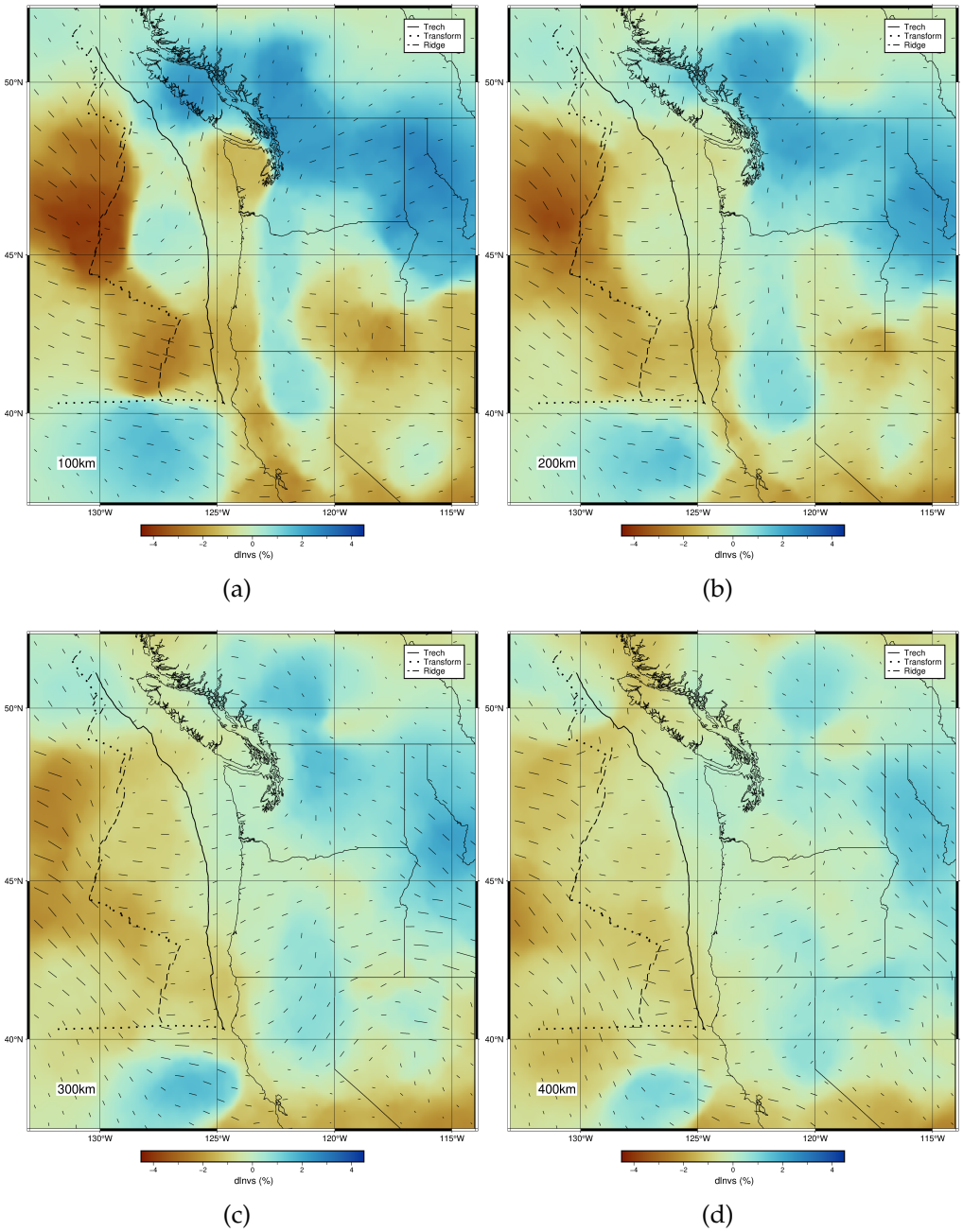

Figure 4.9: Horizontal slices of the RjMCMC inversions with results displayed at 4 depth intervals: (a) 100km, (b) 200km, (c) 300km, and (d) 400km depth. Thin black lines are the USA and Canadian coastline, and USA state boundaries. Colour-scale represents velocity perturbation with reference to AK135 velocity model (Kennett et al., 1995). Hexagonal symmetry axis are plotted as quivers and scaled to magnitude. Thick black lines are offshore tectonic boundaries corresponding to the key in the top right corner.

As with the deterministic inversion, the RjMCMC inversion model displays a consistent region of low velocity anomalies down to 300km depth beneath the mid ocean ridges, characterised by velocity perturbations between -4.5% and -2%. The magnitude of the anomalies decreases with depth and is greater along the JDF ridge compared withe the Gorda ridge section, showing good agreement with the deterministic inversion. The low velocity observed beneath the Gorda micro-plate observed in the deterministic inversion is also present here. The JDF micro-plate does not have sufficient confidence to be interpreted.

The North/South trending high velocity anomaly associated with the down-going JDF slab is also observed in this model as a continuous feature down to 200km. Beneath 200km the high velocity anomaly is resolved in the North and South but with a gap located just South of the Washington/Oregon border (45°N). To the North and South the slab is well resolved as a steep Eastward dipping low velocity anomaly and in a region of higher confidence, whereas the central area does not have sufficient model confidence to ascertain the validity of the gap in this model. In Northern California, the low velocity anomaly is imaged with confidence to a depth of approximately 400km, whereas beneath Washington it is only visible to ~250km.

The North/South, fast/slow divide along central Idaho and Oregon is observed in the back-arc for the deterministic inversion is present for the RJMCMC inversion. The slow velocities seen beneath Southern Idaho and Northern Nevada are confidently resolved down to 150km depth. In the North of the back-arc beneath Idaho and Western Montana, a large high velocity anomaly is present and confidently resolved to a depth of 500km. This is the most consistent anomaly in the model and correlates well with the deterministic results.

Along the Gorda ridge section, the anisotropic vector is orientated ridge perpendicular, for the Gorda micro-plate this trend continues from ridge to trench for the uppermost 200km. On the Pacific plate side of the ridges, the anisotropic vector is oriented parallel/sub-parallel to APM where confidently determined.

Within the confidently resolved sections of the down-going slab, the vector is mostly parallel to the strike of the feature. In the North, the vector within the slab is dipping vertically whereas to the South the vector dips are sub-horizontal. On the Southern tip of the slab, a case could be made for a rotational pattern around the slab edge. However the model confidence is not high enough to say with any confidence.

Within the high velocity anomaly beneath Northern Washington, Idaho, and

Montana, the anisotropic vector is parallel to the North American APM for the upper 150km. At depths greater than this, the vector rotates to be aligned North-West/South-East with this orientation present down to 400km.

4.4 Comparison with Isotropic Models

Overall the anisotropic and isotropic models are very similar for the deterministic inversion. The major discrepancy is, in the anisotropic model the low velocity anomaly beneath the JDF ridge is of higher amplitude. For the isotropic model, the Gorda ridge has an equivalent amplitude at 100km depth and with increasing depth down to 300km the Gorda ridge displays a higher velocity perturbation than the JDF ridge.

The amplitude of the high velocity anomaly identified as the JDF slab is has higher amplitude within the isotropic inversion which also appears to slightly increase its thickness in the East-West direction. The high velocity anomaly beneath Northern Washington and Idaho is also seen to extend further South at 300km in the isotropic model when compared to the anisotropic.

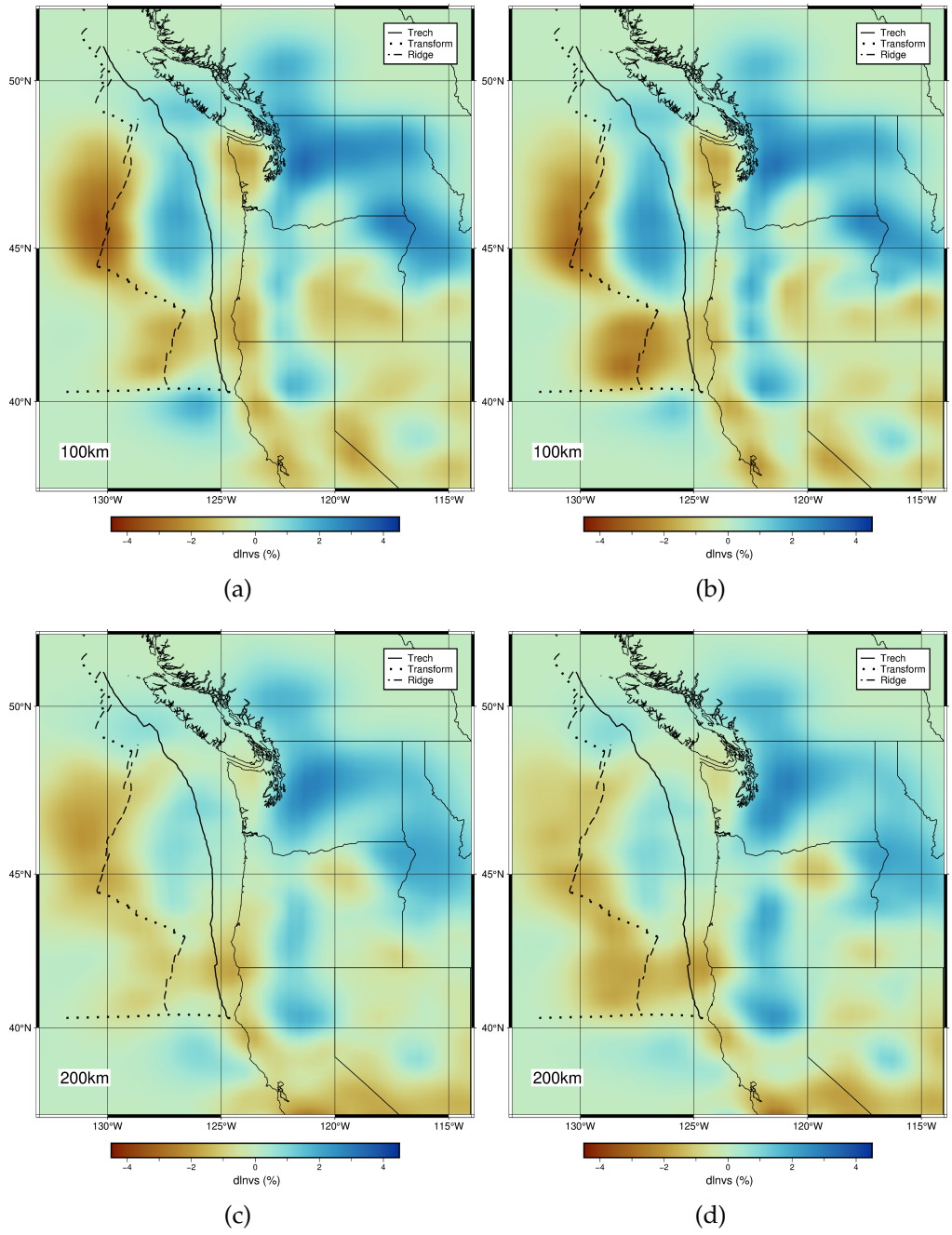

Figure 4.10: Horizontal slices of the Deterministic anisotropic and isotropic inversions with results displayed at 2 depth intervals: (a) 100km anisotropic, (b) 100km isotropic, (c) 200km anisotropic, and (d) 200km isotropic. Thin black lines are the USA and Canadian coastline, and USA state boundaries. Colourscale represents velocity perturbation with reference to AK135 velocity model (Kennett et al., 1995). Thick black lines are offshore tectonic boundaries corresponding to the key in the top right corner.

As with the deterministic inversion, the RJMCMC inversion results are broadly similar between the isotropic and anisotropic inversions. The isotropic inversion shows higher amplitude velocity perturbations on all the features identified in the anisotropic results. The isotropic RJMCMC was closer to convergence than the results from the anisotropic modelling so a direct comparison may not be appropriate. As the depth increases through the model, the size of the isotropic velocity anomalies is consistently larger than the anisotropic model and with greater magnitude of perturbation.

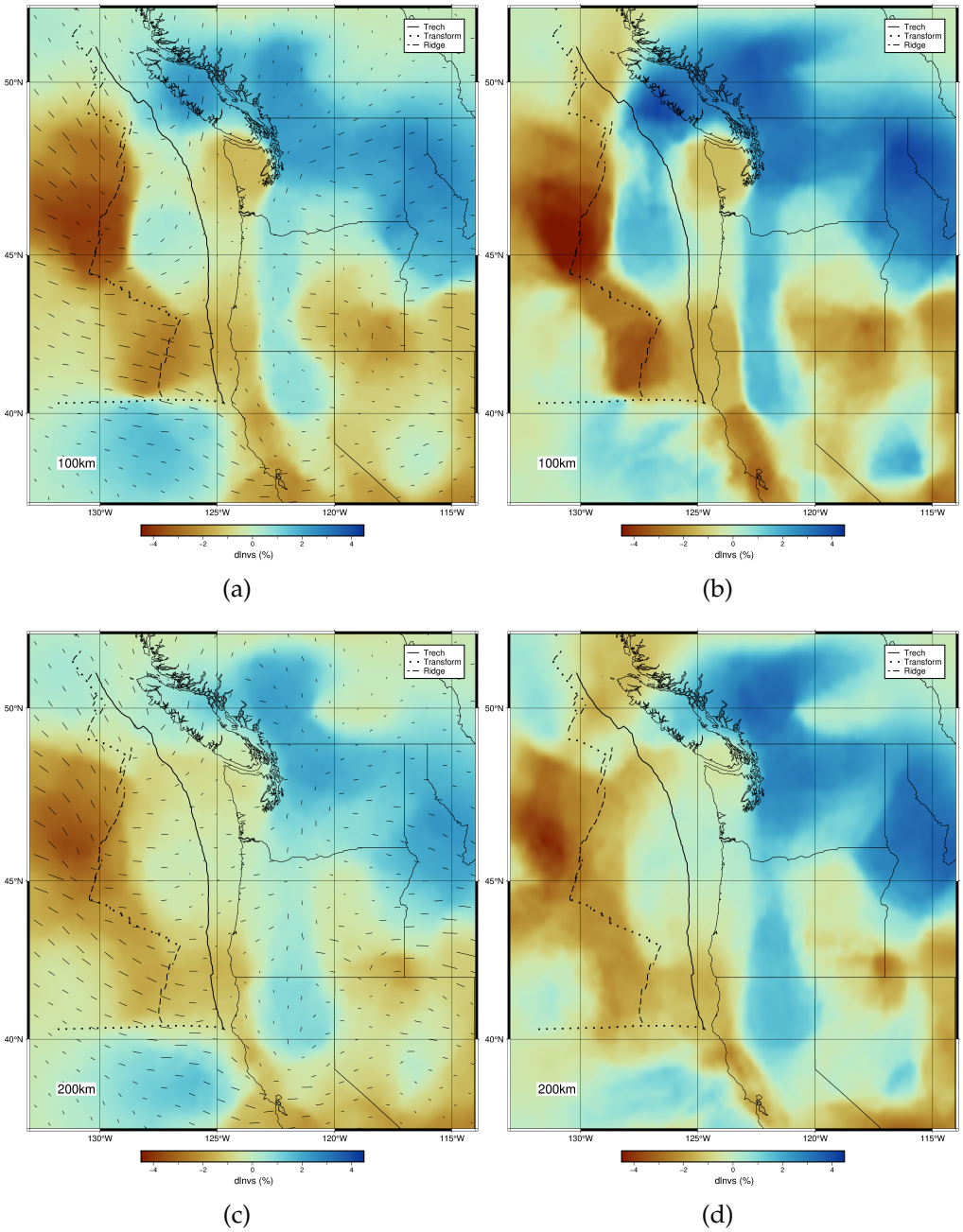

Figure 4.11: Horizontal slices of the stochastic anisotropic and isotropic inversions with results displayed at 2 depth intervals: (a) 100km anisotropic, (b) 100km isotropic, (c) 200km anisotropic, and (d) 200km isotropic. Thin black lines are the USA and Canadian coastline, and USA state boundaries. Colourscale represents velocity perturbation with reference to AK135 velocity model (Kennett et al., 1995). Thick black lines are offshore tectonic boundaries corresponding to the key in the top right corner.

5

Discussion

When comparing the results of this study with those of previous studies, the focus will be on the deterministic inversion. Although the stochastic inversion results were similar, too small regions of the model fall within the confidence regions to infer larger mantle flow processes. As previously discussed, the anisotropic vector orientation is assumed to align with the the faster a-axis of Olivine LPO's and be a proxy for maximum shear direction. Due to the proximity to oceanic ridges, the asthenosphere is expect to be lacking in volatiles due to processes at the ridges (Russo, 2009). Recent studies by Wang et al., 2024, found evidence for very localised sub slab melting, but in an extremely thin region of approximately 3km thickness beneath the oceanic lithosphere. Therefore sub-slab melting is not expected to be widely distributed. A, C and E LPO types are assumed for all regions except small parts of the mantle wedge where dehydration may have lead to serpentinisation and/or B-type fabrics (Russo, 2009).

Direct comparisons with other studies are not possible, with almost all previous work such as Martin-Short et al., 2015, Bodmer et al., 2015, Eakin et al., 2010 and Currie et al., 2004 focused on SKS waves, a shear wave that traverses the Earth's outer core as a P wave (Storchak et al., 2003). The results of these studies are presented as an averaged splitting measurement for each station and therefore the source of the anisotropy cannot be directly determine. Possible sources could include: (Eakin et al., 2010):

- Fossilised anisotropy in the continental and oceanic lithosphere
- The mantle wedge
- The subducting lithosphere

- The sub-lithospheric mantle

For this study however, it is possible to observe how the anisotropy varies with depth. To allow comparison with SKS splitting studies, it is important to rule out fossilised anisotropy within the lithosphere as a major contributor to delay times in. Considering the delays of >1 second observed, a mean S-wave velocity of $4.5km^{-1}$, creating large delays would require a 100km thick mantle region with anisotropy of 5% (Currie et al., 2004). Therefore it is appropriate to attribute the large delays in SKS splitting studies to mantle sources and allow comparison with this study.

5.1 Oceanic Plates and Mantle

As discussed in section 4.2.2, the regions of the model corresponding to the mid ocean ridge systems (MOR) are characterised by low velocity anomalies. The lowest velocity perturbation is centralised on the Southern section of the JDF ridge. This very close to the location of the Axial seamount (46°N, 130°W), the latest sub-marine volcano in the Cobb-Eickelberg seamount chain. It is proposed that this is the location of the Cobb hotspot, with lava samples found to comprise 40% hotspot composition and 60% mid ocean ridge basalt (Arnulf et al., 2018). The anisotropic vectors are dipping sub vertically which would be consistent with mantle plume up-welling (Blackman et al., 1993). The depth of the anomaly beneath the JDF ridge is only prominent to a depth of 200km and not visible into the deeper mantle. It is therefore more likely that this anomaly is more consistent with asthenospheric up-welling and partial melt relating to spreading activity at the MOR. Studies by Team, 1998 using Rayleigh waves observed primary melting at MORs begin at 100km depth and partial melting occurs down to 150km at the East Pacific Rise. This is more consistent with the model produced in this study.

The anisotropy beneath the Pacific plate in all regions covered by this study are show to be sub-parallel/ parallel to the APM of the Pacific plate. The Pacific plate is an extremely large, competent plate with a much greater velocity ($51mmy^{-1}$ against $19mmy^{-1}$ for the JDF plate). The alignment of anisotropic vectors here are attributed to basal drag from the Pacific plate through viscous coupling with the asthenospheric mantle. Only a shallow region (< 200km depth) Southern edge of the JDF ridge and BFZ show more ridge perpendicular/BFZ along strike parallel alignment. The BFZ accommodates the shear motion between the South of the JDF micro-plate and the Pacific Plate. The

strain along the fracture zone is oriented along strike, with higher plasticity at shallower depths (Faccenda and Capitanio, 2013) causing alignment of the LPO with the strike of the right lateral transform fault in the upper 150km. For depths greater than this, the APM of the Pacific plate dominates the mantle flow as it has greater coupling with the upper mantle (Long, 2016).

The JDF ridge initially displays ridge perpendicular anisotropy at latitudes lower than 46°N, and the Gorda ridge displays this in its entirety. The Olivine LPO is expected to form beneath the ridge, with the a-axis aligned with mantle divergence at the MOR (VanderBeek and Toomey, 2017). Thus the anisotropic vector is aligned with the spreading direction and relative plate motion (RPM). The Northern part of the JDF ridge however does not display this ridge perpendicular anisotropy from 46°N and northward, and is more aligned to the Pacific plate APM. It is possible that for the North of the JDF micro-plate mantle flow is more heavily dominated by the Pacific plate.

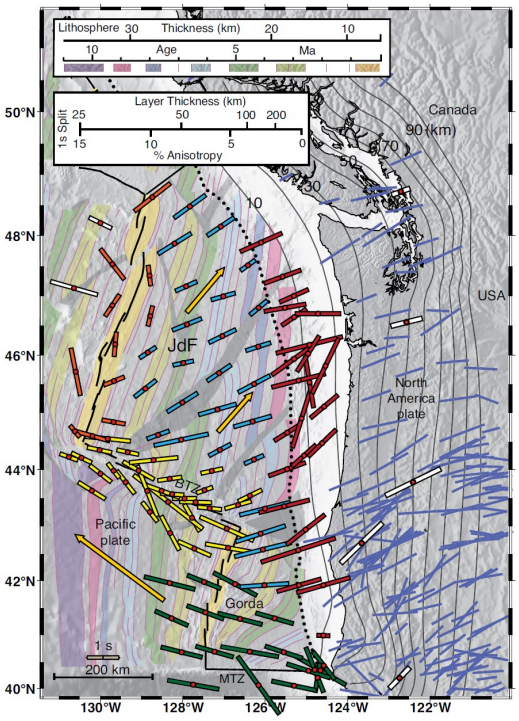

Figure 5.1: SKS splitting results from Bodmer et al., 2015. Coloured bands represent lithosphere age as determined by magnetic anomalies. The thick bars represent SKS splitting results, colour coded by the distinct regions identified. Bars are aligned to fast splitting direction and scaled by delay time. The Yellow arrows are absolute plate motions with reference to a hot spot.

Within the JDF and Gorda micro-plates, the orientation of anisotropy does not vary with depth apart from as mentioned above, but magnitude decreases with depth. The results are largely in agreement with those of Bodmer et al.,

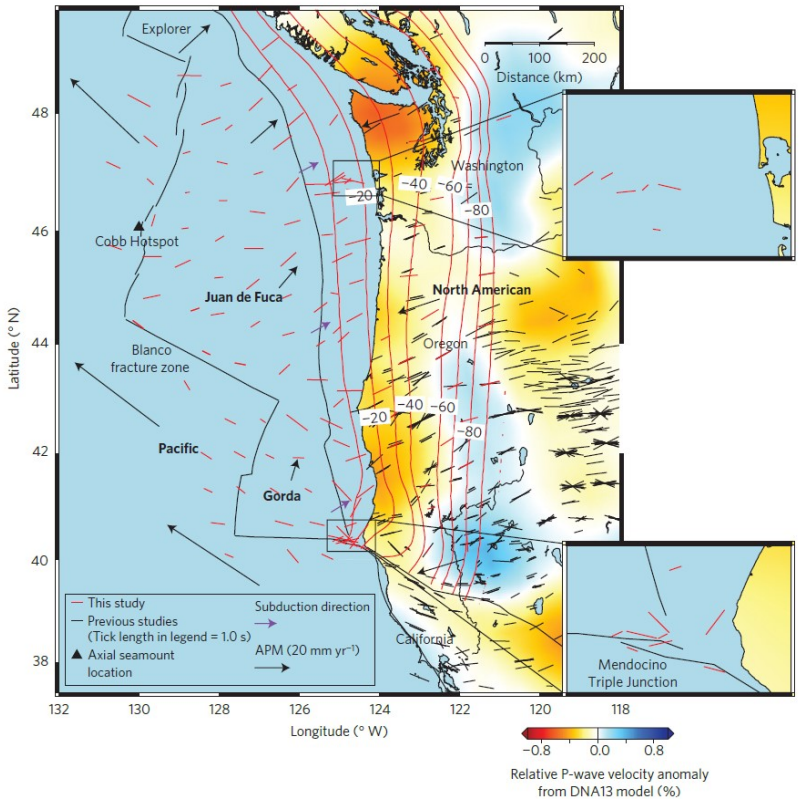

Figure 5.2: SKS splitting results from Martin-Short et al., 2015. Continental region is coloured to represent P-wave velocity anomaly tomography averaged over the depth range 100-400km. Red bars represent averaged splitting results at stations scaled by magnitude of delay time, black bars are from previous studies. Black arrows are APM scaled by magnitude, purple arrows are subduction directions. Black lines are plate boundaries with red contours are slab depth in km.

2015 and Martin-Short et al., 2015 displayed in 5.1 and 5.2 respectively. However as these are SKS splitting results, they do not detect the rotation from shearing direction in the BFZ to Pacific APM with increasing depth. Similarly to Bodmer et al., 2015, the intra micro-plate splitting directions are separated into two regions. One covering the entire JDF micro-plate and the northern most section of the Gorda micro-plate, and a second containing the rest of the Gorda micro-plate. The separation of these two differing zones approximately follows the strike of the BFZ.

The JDF micro-plate initially displays ridge perpendicular at the South, and display a clockwise rotation to become sub-parallel to the JDF APM most prominent at shallower depths (orange arrows in figure 5.1). As the oceanic lithosphere moves from ridge to trench, it cools and thickens following the half space cooling model (Turcotte and Schubert, 2002). At the subduction zone the JDF slab is

approximately 40-50 km in thickness (Eakin et al., 2010) and between 8-10 Myr old (Bodmer et al., 2015), the age of the plate is shown as coloured bands in figure 5.1. Calculations by VanderBeek and Toomey, 2017 suggest that by 2.5Myr, 10km of the upper mantle becomes frozen into the lithosphere. This in turn creates simple shear in the upper mantle up to a depth of 100km (VanderBeek and Toomey, 2017). Simple shear creates the olivine LPO, oriented to APM on the JDF plate, and causes the shallower rotation of the anisotropic vector seen in the model. As the lithosphere continues towards the Cascadia trench, it cools and thickens further, increasing its influence on the upper mantle and aligning the fabric further.

The Gorda micro-plate, unlike the JDF micro-plate, has consistently oriented anisotropic vectors from ridge to trench, apart from the very Northern most section. As discussed in section 2.2 the JDF ridge is spreading 32mm/yr faster than the Gorda Ridge causing the Gorda micro-plate to undergo internal deformation, North-South shortening, clockwise rotation and possible break-up (Ismat et al., 2022). It is proposed that the Gorda micro-plate has little to no entrained sub-slab mantle and is simply a broad shear zone between the more rigid and competent JDF/Pacific plates (Bodmer et al., 2015). The direction of the anisotropic vector is unaffected crossing over the MOR and MFZ to the West and South respectively into regions beneath the Pacific plate, again suggesting the Gorda micro-plate motion has little influence on underlying sub-lithosphere mantle (Mosher et al., 2014). The mantle flow patterns beneath the weakly coupled Gorda micro-plate are instead aligned to Pacific-JDF plate relative plate motion (Bodmer et al., 2015). The lack of coupling with the mantle and intense plate deformation are possible precursors to complete plate break-up and detachment from the rest of the JDF plate system (Mosher et al., 2014 and Bodmer et al., 2015).

5.2 Onshore

The most striking feature in the tomographic model is the consistent North-South striking high velocity anomaly, which is interpreted as the subducting JDF plate system. The subducting slab is expected to be imaged as a faster velocity anomaly, with a cooler, denser slab of oceanic lithosphere entering warmer upper mantle asthenosphere. The anomaly also terminates at a similar latitude to the MTJ as to the South of this no subduction occurs and a slab window is present (Schellart et al., 2010). The Southern section, where the cross sectional image of the slab is more defined, it is dipping to the East at approximately 60°. Due to the presence of a high velocity anomalies in the North of the back-arc, determining the slab dip is more challenging.

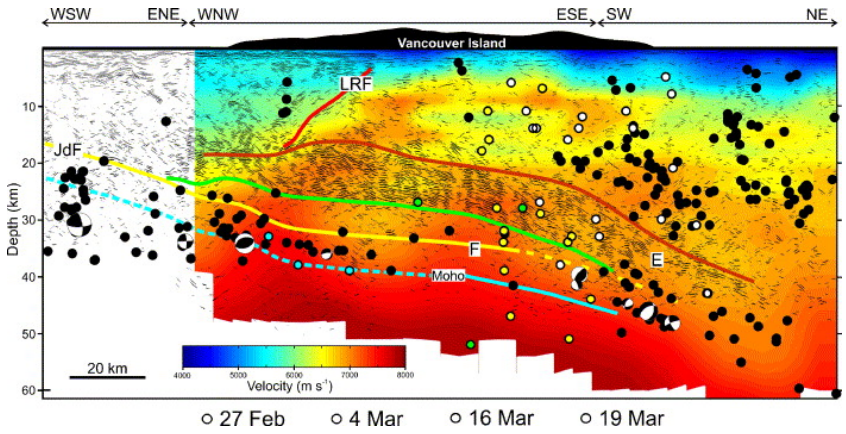

Figure 5.3: Interpreted seismic reflection profile beneath Vancouver Island to a depth of 60km. Orientation of the Line is shown by annotations above. Line begins on the left at (126°W, 47°N) to (123°W, 47°N). The coloured section is a superimposed P-wave tomography model. Yellow line represents the top of the subducting plate, Brown and Green lines are the top and base of an identified reflector respectively, Red is the Leech River Fault and Blue is the Moho. Filled black circles represent earthquake hypo-centres and white circles are events from 2003. (Calvert et al., 2006)

The shallow zone of subduction is not resolved in this study but the initial subduction of the JDF plate is known to be relatively shallow (10° to 15°) (DiPietro, 2018). Figure 5.3 displays the extremely shallow dip of the slab in the very upper mantle beneath Vancouver Island obtained from an active source seismic survey (Calvert et al., 2006). In this section the slab is only imaged to a depth of 40km and the very shallow dip of initial subduction is apparent. The subducting slab is imaged approximately 300km from the Cascadia trench for a depth of 100km, this implies an average dip of 18°. Tomographic modelling of the JDF plate by Cheng et al., 2017 found the dip angle steeping in a zone between 50km and 75km, whilst Han et al., 2016 observed initiation of plate bending occurs 40km from the trench. Therefore extensive slab rollback must be occurring in the region between 40km and 100km where the dip transitions from <15° to the steeper 60° observed in this study. This is consistent with what is expected for a young (<10 Myr) and warm oceanic plate subducting with a slow convergence rate (Martin-Short et al., 2015). The role significant steepening and rollback of the slab plays in mantle flow is dependent on the continuity of the slab with depth. A continuous slab would cause over pressure by blocking mantle flow and lead to sub-slab extension parallel to the trench (Faccenda and Capitanio, 2013), whereas this would not be expected with a highly fragmented slab.

For the upper 200km the subducting slab is clearly imaged as a single anomaly from latitudes level with the MTJ in the South, to British Columbia in the North. Along strike, the slab anomaly has considerable heterogeneity in width, amplitude and anisotropic vector orientation. At 210km depth, the slab is no longer a continuous feature with a break located at approximately 45°N. Whether or not this break in the down-going slab is a real feature or just an artifact of the inversion is a highly debated topic. Previous tomographic studies of the Cascadia subduction zone are in agreement that the slab gap is present beneath central Oregon (Gao and Shen, 2014, Obrebski et al., 2011, Schmandt and Humphreys, 2010) with Schmandt and Humphreys, 2010 observing in both P and S wave inversions. The tomographic modelling of Hawley et al., 2016 however observes a continuous yet still highly variable anomaly. Furthermore Tauzin et al., 2016 used receiver functions, to observe a continuous plate in this region, however with a marked reduction in S-wave velocity. Seismic reflection studies of the JDF plate system offshore by Han et al., 2016 found that greater faulting of the JDF plate occurs off the coast of Oregon than elsewhere. This would lead to more hydration and serpentinisation, explaining the marked reduction is S-wave velocity relative to the rest of the feature. From the results of

this study, it would appear that there is indeed a gap or tear in the subducting slab beneath central Oregon, however it cannot be determined that this is not a product of the lower S-wave velocities identified by (Tauzin et al., 2016). Another possible slab tear is proposed by Mullen and Weis, 2015 between the JDF and Explorer micro-plates. This however would occur too far North to be resolved by the tomographic model, yet its effect on mantle flow would be present in the model.

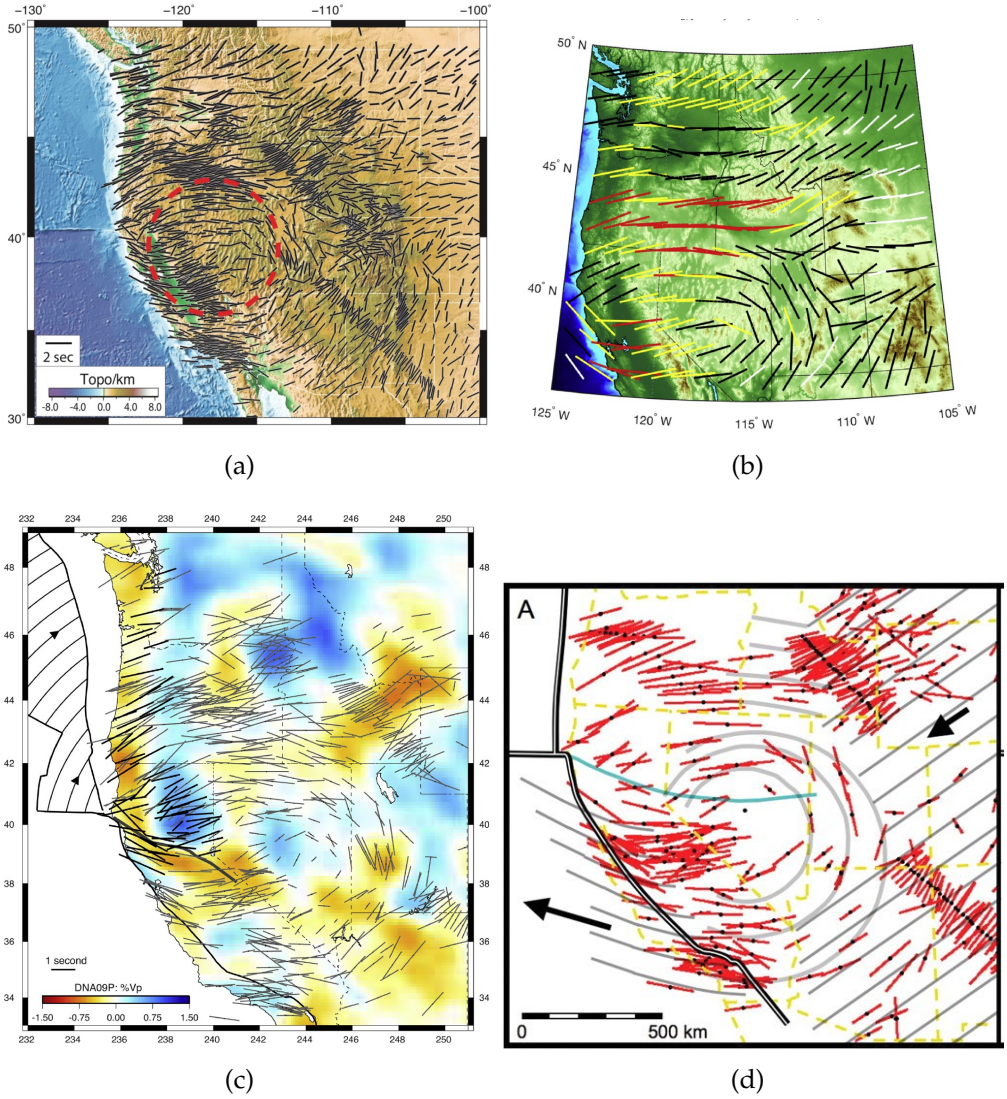

Figure 5.4: (a) SKS splitting results from Becker et al., 2012 and presented by Zhou et al., 2018, SKS splitting displayed as bars and scaled by delay time. Background topography from ETOPO1.0. (b) SKS splitting results from the database of Liu et al., 2014. Results are displayed as bars and colour coded by delay magnitude: red - δt > 1.6s, yellow - 1.6s > δt > 1.3s, black - 1.3s > δt > 1.0s, and white - δt < 1.0s (c) SKS splitting results from Eakin et al., 2010, SKS splitting displayed as black bars and scaled by delay time. Grey bars are SKS results from previous studies. Background is the vertical average velocity anomaly P-wave model from Obrebski et al., 2011. Black arrows represent APM for the JDF and Gorda micro-plate. (d) SKS splitting results from Zandt and Humphreys, 2008. SKS splitting displayed as red bars and scaled by delay time.

The splitting directions in the sub-slab mantle between trench and coastline are fairly consistent with those of previous studies (figure 5.4). North of the BFZ, vectors align approximately trench perpendicular which suggests in this region that good coupling is present between the down-going lithosphere and asthenosphere. Figures 5.4 (a), (b), (c) and (d), are previous SKS splitting studies. An immediate difference between the SKS splitting and the models discussed in section 4.2.2 is the apparent smoothness of trends in SKS splitting data. The SKS splitting results are presented as the stacked splitting parameters (δt and ϕ per station (Eakin et al., 2010). The un-stacked data is much more variable, with a wide range of splitting directions observed close together, and is indicative of multiple layers of anisotropy or abrupt changes in the direction of LPO orientation (Martin-Short et al., 2015). Therefore the results the present are a representative average per station.

In-land towards the subducting slab and into the back-arc region, the picture become much more complex than that in the oceanic setting of the region. Rotation of splitting directions is observed in all the studies with results displayed in figure 5.4, centered just to the Southern extent of the subducting slab. For this study, the rotational behaviour of the anisotropic vector is most prominent in the shallowest 200km of the model. A major discrepancy with this study's results is the North-South orientation of the anisotropic vector in the sub-lithospheric mantle at the Southern 200km of the subducting slab. This orientation would suggest that there is a region trench parallel sub-slab extension and mantle mantle flow. Long, 2016 theorised that localised serpentinisation or a possible conversion to B-type LPO is responsible for this, yet the sub-slab mantle is expected to be dry as dehydration occurs much shallower depths (Han et al., 2016).

Numerical simulations by Faccenda and Capitanio, 2013 for a sinking slab, with slab rollback, produce a trench normal over-pressure in the sub slab mantle. Over-pressure then leads to trench parallel extension. In the numerical model for a 300km half width plate, two orthogonal anisotropic domains form in the sub-slab mantle displayed in figure 5.5 (Faccenda and Capitanio, 2013):

1. A 100km thick trench perpendicular upper entrained mantle layer
2. A trench parallel sub-slab region

In the model produced in this study, there is trench parallel flow in the upper 200km and the upper entrained flow is not observed here as with Faccenda and Capitanio, 2013. A possible explanation is that this is beneath the subducting Gorda micro-plate section, which as discussed earlier has very weak coupling

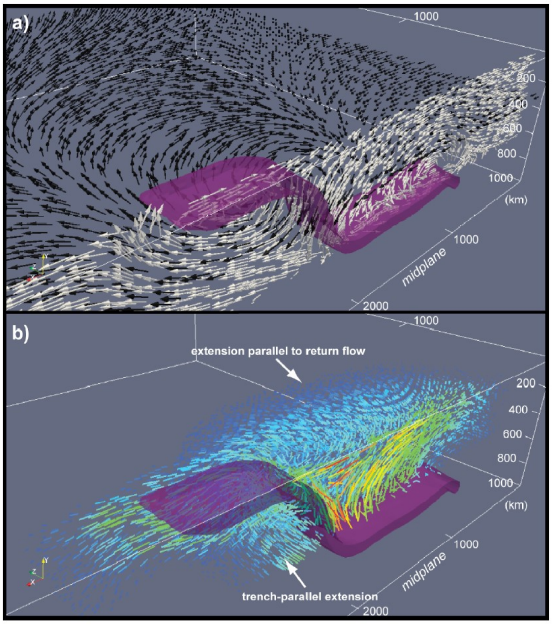

Figure 5.5: Numerical model for a subducting slab with 300km half width Faccenda and Capitanio, 2013. (a) The velocity field with black arrows displaying the toroidal flow at 300km depth and white arrows displaying the poloidal component of flow at 100km from the slab centre. (b) The orientation of maximum finite strain axis.

between the lithosphere and asthenosphere (Bodmer et al., 2015), as shown by the lack of alignment to APM in the offshore region. Therefore this layer of entrained mantle observed in the simulation of Faccenda and Capitanio, 2013 may not be present beneath the Gorda micro-plate. This is further backed up by the sub-slab mantle beneath the JDF micro-plate to the North displaying anisotropic vectors parallel to APM for comparable distances from the trench. Suggesting that in this region, there is greater viscous coupling between lithosphere and asthenosphere.

The numerical modelling of Faccenda and Capitanio, 2013 predicts large scale return flow in a toroidal pattern from behind the slab to the mantle wedge (black arrows in figure 5.5). The presence of this toroidal flow in Southern Cascadia is debated, with Zandt and Humphreys, 2008 and Zhao and Hua, 2021 agreeing with the toroidal flow occurring. Bodmer et al., 2015 and Martin-Short et al., 2015 both did not find evidence for toridal mantle flow, however the result produced did not show any trench parallel anisotropy as seen in this study. Eakin et al., 2010 proposed that there was localised flow around the Southern edge of the Gorda micro-plate (figure 5.6) with entrained flow beneath the plate. Again the entrained flow is not observed in the upper 200km in this model.

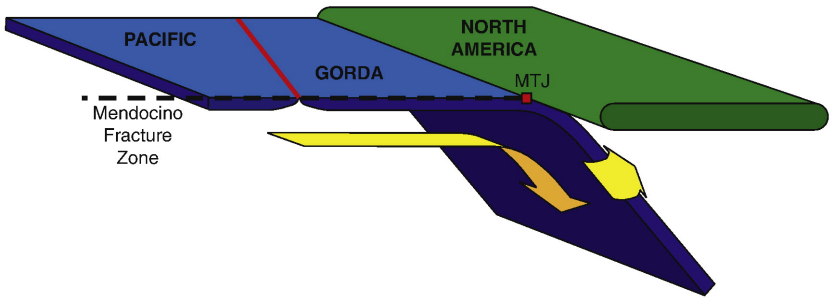

Figure 5.6: Proposed localised corner flow model proposed by Eakin et al., 2010. Yellow arrows represent the direction of mantle flow. Red line is the Gorda ridge.

Having large scale toroidal flow around the slab edge does not necessarily require a continuous slab at depth, so long as it is continuous in the shallow mantle and viscosity jump is present at the mantle transition zone (410km) (Long, 2016). In the upper 200km where the gap is evident from tomography, there is a sharp change of anisotropic vector direction from North-South to East-West. Löberich et al., 2021 proposes that return flow through this slab gab is present. Schmandt and Humphreys, 2010 relates the slab gab to the along strike variation in volcanic eruptions observed in Oregon (more volume of erupted material) compared to Washington. The issue is that the East-West alignment is only present in the upper 200km where as the slab gap is imaged below 200km. Possibly all of the East-West oriented anisotropic regions could just be simple poloidal corner flow in the mantle wedge. Therefore the slab gap is present in the tomography model produced in this study but return flow through the gap as suggested by Löberich et al., 2021 is not directly observed.

Another possible explanation of this rotational pattern observed could simply be the reorganisation of mantle flows in the vicinity of the MTJ. With the Pacific plate APM in a North-East direction and the North American plate APM to the South-West. Also present is a large shear zone related to the San Andreas Fault. The orientation of the anisotropic vectors rotate from Pacific APM off the coast of California to North American plate APM beneath Nevada with a transition occuring beneath California.

The proposed slab tear by Mullen and Weis, 2015 between the Explorer and JDF micro-plate is not observed tomographically, and should be located in Northern Vancouver Island. However if present then slab parallel flow should occur from rollback induced over-pressure and flow through the tear. In Southern British Columbia and Northern Washington, there is North-South oriented anisotropy observed in the upper 150km. There is also geo-chemical evidence

in lava erupted in the Garibaldi Volcanic Arc. From the slab edge in the North, moving southward, trace elements in the lava become more indicative of a depleted mantle and more slab derived melt (Mullen and Weis, 2015) suggesting slab parallel flow. Figure 5.7 displays a diagram of mantle flow through the slab tear and along the strike of the slab. Our model does not have coverage far enough North to observe any toroidal pattern to the North of Vancouver Island, however the along strike flow could be evidence that this is occurring.

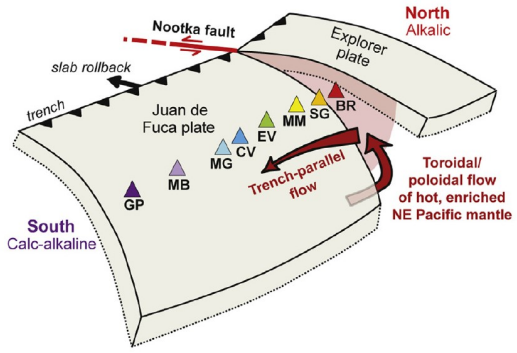

Figure 5.7: Mullen and Weis, 2015 theorised along slab flow of mantle material and change of lava composition. Triangles represent volcanoes in the Garibaldi chain with Red representing a Alkalic composition and transitioning to Calc-alkaline in the South.

With a large region of trench parallel flow, and a rotation of anisotropic vectors to the South of the Gorda micro-plate, it is plausible that toroidal flow or at least some localised flow around the Gorda micro-plate is occurring. The subducting plate is rolling back at 33mm/yr (Schellart et al., 2010), and has been for at least 12 Myr (Ford et al., 2013), then the sub-slab mantle must have to move to accommodate this. The modelling of Faccenda and Capitanio, 2013 observes trench normal anisotropy in the back-arc and mantle wedge. To the East of the slab in the mantle wedge, the anisotropic vectors are consistently sub-normal to the slab. The anisotropic vectors in the mantle wedge are sub horizontal, to dipping slightly westward which would be expected of poloidal flow in the mantle wedge (Faccenda and Capitanio, 2013). No abrupt change in orientation in the mantle wedge associated with serpentisation or change to B-type LPO was observed. The results of Tauzin et al., 2016 show that hydration of the mantle wedge is limited to the upper 60km.

In the back-arc, the tomographic model is split between high velocity anomalies to the North and low velocity to the South. This transition occurs approx-

imately along the boundary of the HLP/Great Basin and Ranges to the south and the Blue Mountains/Columbia Plateau to the North (figure 5.8). The slow Northern Basin and Ranges and fast Colorado plateau is in agreement with the tomography results of Obrebski et al., 2011, which found this large region of slower velocity to a depth of 150km for the Western United States.

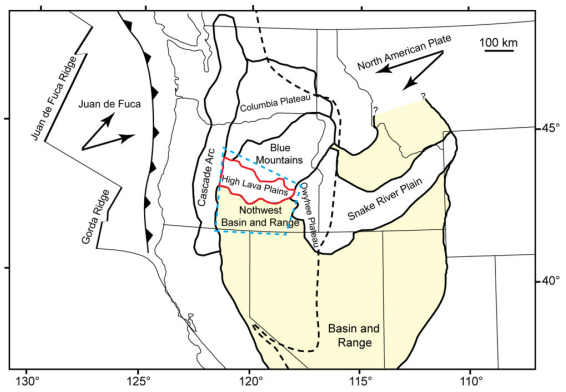

Figure 5.8: A map of the tectonic provinces of the Western United States of America (Ford et al., 2013). Black dashed line indicates the Western extend of the Proterozoic North American Craton.

The Basin and Ranges is known to have high heat flux, thin crust and high elevations. It has possibly been thinned by either extension or by lithospheric drip with low velocities expected here. The lower velocities seen here are possibly related to the toroidal corner flow bringing warmer sub-slab mantle material and inducing melt (Zhao and Hua, 2021). In Southern Idaho, there is a small shallow section of North-South oriented anisotropy. This may represent the farthest East that any possibly component of the toroidal flow at the southern edge of the plate is observed. Hawley et al., 2016 proposed that beneath the oceanic lithosphere there the is an accumulation of a thin weak layer which can only be imaged with teleseismic waves when the slab geometry changes and is observed as a high conductivity region in electrical studies (Hawley et al., 2016). This would be observed in the model as a low velocity anomaly in the upper 100km beneath the fore-arc, however Bodmer et al., 2020 dismisses this as a modelling artifact. If the upward flow of this material is greater than the drag from the subducting lithosphere then a zone of accumulation occurs beneath the bending slab. The aforementioned slab rollback induced toroidal flow forces this material into the back-arc to where this low velocity anomaly is observed (Hawley et al., 2016). The presence of this partial melted material would explain the lower velocities and volcanic activity observed in this region. Although the Northern Basin and Ranges has a high heat flux (average $75mW/m^2$), it is not as high as would be expected for asthenospheric up-welling (Hawley et al., 2016). This is again more evidence for flow around the Southern edge of the Gorda micro-plate and into the back-arc.

To the South East of the model, a 150km diameter circular high velocity anomaly, continuous throughout the model is observed. Surrounding this region, the anisotropic vector becomes weaker and more variable. Obrebski et al., 2011 suggests that it is part of the old Farallon slab, or a detached section of the subducting Gorda micro-plate. However West et al., 2009 attributes this to lithospheric dripping (figure 5.9), with the anomaly identified as the Great Basin Drip (GRB). This could be a large part of eclogitised lower crust, which was overlying less dense mantle asthenosphere (Beall et al., 2017). When localised strain conditions triggered instability in the lower crust, the ecolgitised portion became unstable and began to sink into the lower mantle (West et al., 2009). Low and variable anisotropic vector results in this region could be caused by vertical mantle flow, for which there is some evidence for in the upper 200km of the model. The anomaly is frustratingly located on the boundary of the model, without increasing the model boundaries it is extremely challenging to attribute

this anomaly one way or another. However the lithospheric drip argument would help explain the lower velocity anomaly in the South of the back-arc and extension of the Basin and Ranges province. This would cause a thinner crust and lead to mantle up-welling and partial melt, reducing seismic velocities.

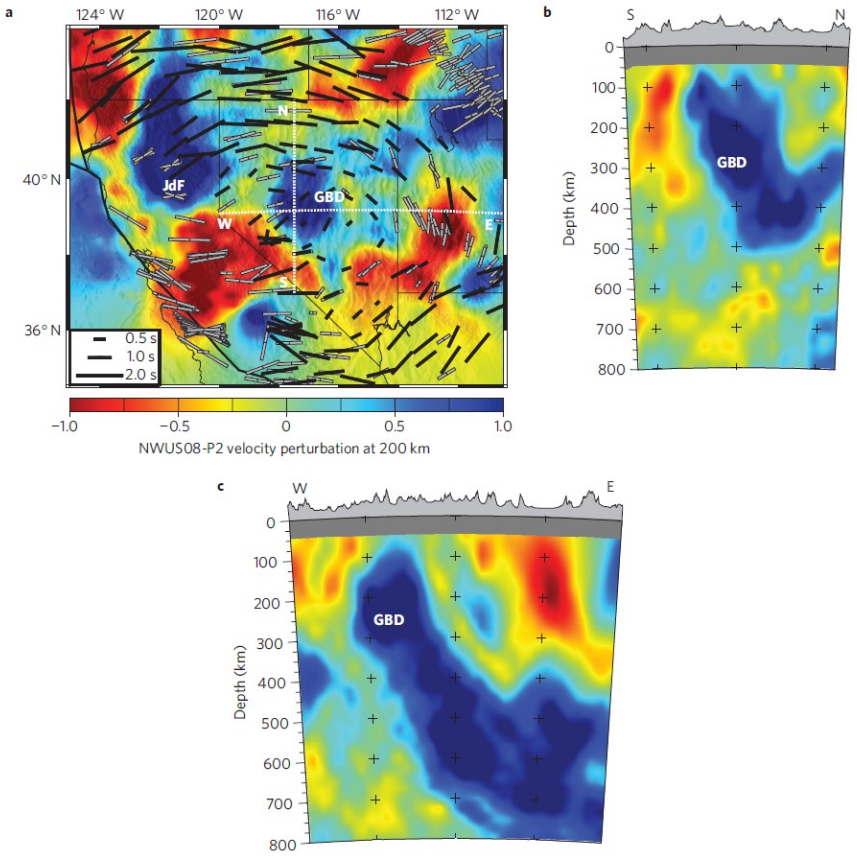

Figure 5.9: (a) P-wave tomography model slice at 200 km depth (West et al., 2009). Shear-wave splitting results are plotted as bars with magnitude scaled to delay times. White dashed lines denote cross section locations displayed in (b) and (c). JdF and GBD denote the anomalies related to Juan de Fuca plate and Great Basin Drip respectively. (b) Cross section along North South line of (a). (c) Cross section alone East West line of (a).

The sharp boundary between North and South in the back-arc does correlate extremely well with the tectonic provinces in figure 5.8. The Blue Mountains and Columbia Plateau to the North (corresponding to high velocity anomalies). The Blue Mountains are accreted terranes, which compared to the Basin and Ranges have undergone much less extension (Ford et al., 2013), meaning that less asthenospheric up-welling occurs, explaining the variation in velocity anomalies. Despite the extension in these regions being of a lesser extent than seen in Basin and Ranges, extension still occurred. Schmandt and Humphreys, 2010 proposed that this high velocity feature is the Farallon slab which has remained attached to an accreted terrane. The models produced in this study would have to be extended further Eastward in order to fully asses this claim. It is more plausible that a combination of lithospheric drip and toroidal corner flow are the cause of low velocities in the Southern back-arc whereas in the North is closer to the Proterozoic North American Craton. Tomography models from Obrebski et al., 2011 with a much larger model observe this feature as part of the much larger low velocity anomaly seen under the North American Craton.

It seems that across the continental region of the subduction zone, the anisotropic vectors provide evidence for both end member subduction flow types displayed in figure 5.6. Flow around the edge of the South of the Gorda plate, trench parallel flow and low S-wave velocities observed in the Southern back-arc are expected from toroidal flow presented by Faccenda and Capitanio, 2013. Meanwhile further North, the entrained mantle beneath the subducting slab is found to be trench perpendicular, with poloidal 2D corner flow present in the mantle wedge as expected from the other end member of mantle dynamics at subduction zones (Long, 2016). As is often the case, the real world situation does not belong to one simplified model and instead is much more complex.

Finally, moving Eastwards further into the back-arc, Nevada and Montana, away from the subducting plate system where the Western edge of the Proterozoic North American craton is present, the shallower anisotropy begins to align back to the North American APM. The lithosphere in Eastern Idaho and Eastward is approximately 200km thick (Currie and Yu, 2023) compared with 60km in the in the Basin and Ranges. It is expected that the large continental mass has a thicker region of entrained mantle with maximum strain oriented sub parallel to APM. This is in agreement with previous SKS studies, as the upper mantle transitions from subduction dominated flow to continental dominated flow.

6

Conclusions and Further Developments

This study has produced large scale tomographic models for velocity perturbations of teleseismic shear waves whilst also retrieving the orientations of mantle anisotropy resulting from LPO alignment of upper mantle minerals. Anisotropic vectors aligned with the hexagonal symmetry axis are a good proxy for the orientation of shear and mantle flow. How the orientation varies with depth as well as lateral position was able to be discussed, whereas with previous SKS studies this was not possible.

Tomographic results for the deterministic inversion were similar to the previous studies of Gao and Shen, 2014, Obrebski et al., 2011 and Schmandt and Humphreys, 2010. Low velocity anomalies were present beneath the mid ocean ridge systems, most prominently in the upper 200km, suggesting the source was asthenospheric up-welling. The subducting oceanic lithosphere was identified as a North-South striking high velocity anomaly beneath Washington, Oregon and Northern California dipping Eastward at 60°. The dip observed is much steeper than the initial subduction angle of 15° (DiPietro, 2018) implying significant steepening and slab rollback. From the tomography, the slab was not a continuous feature with a gap observed at 45°N. In the back-arc, a distinct split was observed with a high velocity North and low velocity South. The low velocity seen in the South is associated with the thin crust and high elevations of the Basin and Ranges province. Evidence for a lithospheric drip was found, with a high velocity anomaly possibly related to detached lower eclogitized crust observed. This could explain the thin crust, however warm asthenosphere

moving around the corner of the slab is another possible source.

The large Pacific plate was found to dominate large regions of the offshore data, with anisotropic vector orientations aligning close to its APM beneath it. The orientation beneath the JDF micro-plate was found to rotate from ridge perpendicular to the APM as it moved from ridge to trench, attributed to thickening lithosphere increasing shearing in the upper mantle. The Gorda micro-plate was found to have little to no influence on the anisotropy in the upper mantle, and instead is accommodating shear between the Pacific and JDF plates.

The picture onshore was found to be much more complex than that beneath the oceanic plates. Evidence for trench parallel anisotropy in the sub-slab mantle at the Southern end of the subducting plate, coupled with a rotation of anisotropic vectors around the Southern Tip of the plate, provide evidence for toroidal flow. The over-pressure caused by slab rollback forces slab parallel extension and toroidal flow around the edge of the subducting slab into the back arc. More trench parallel flow was observed in the Northern most section of the subducting slab, which may be evidence for toroidal flow around the Northern edge of the slab. For the central section of the slab the results were consistent with the sub-slab mantle being entrained beneath the subducting slab.

One option for further study in this area is to include more seismic wave types into the inversion. For body waves, Faccenda and VanderBeek, 2023 outlined methodology closely related to that of VanderBeek and Faccenda, 2021 and VanderBeek et al., 2023, for the joint anisotropic inversion of P and S waves. This method has only been implemented on synthetic data, and it would be interesting to compare results of a joint inversion with the S-wave inversion completed in this study. Secondly, surface wave data should be incorporated into the model. Obrebski et al., 2011 incorporated short period surface waves into the tomographic model. The surface wave data should increase lateral resolution in the shallow portion of the model, for Obrebski et al., 2011 this was <60km, which could help resolve the shallow mantle wedge and possibly very shallow portions of the JDF subducting slab.

Alongside the deterministic inversion, a stochastic inversion was undertaken using the Reversible jump Markov Chain Monte Carlo method. Whilst the results were initially promising and similar to the deterministic inversion, the regions of the model with sufficient confidence were too low to provide a full discussion. However this was an initial inversion attempt and the model had been found to have not reached convergence. Due to the computationally intensive nature of these inversions, it was not possible to increase the number

of iterations for this study. Future studies should be able to run the inversion for more iterations to allow convergence, which should improve the confidence regions.

References

Arnulf, A. F., Harding, A. J., Kent, G. M., & Wilcock, W. S. D. (2018). Structure, seismicity, and accretionary processes at the hot spot-influenced axial seamount on the juan de fuca ridge. *Journal of Geophysical Research: Solid Earth*, *123*, 4618–4646.

Aster, R. C., Borchers, B., & Thurber, C. H. (2018). *Parameter estimation and inverse problems*. Elsevier.

Beall, A. P., Moresi, L., & Stern, T. (2017). Dripping or delamination? a range of mechanisms for removing the lower crust or lithosphere. *Geophysical Journal International*, *210*, 671–692.

Becker, T. W., Lebedev, S., & Long, M. D. (2012). On the relationship between azimuthal anisotropy from shear wave splitting and surface wave tomography. *Journal of Geophysical Research: Solid Earth*, *117*.

Becker, T. W., Chevrot, S., Schulte-Pelkum, V., & Blackman, D. K. (2006). Statistical properties of seismic anisotropy predicted by upper mantle geodynamic models. *Journal of Geophysical Research: Solid Earth*, *111*.

Bernard, R. E., Schulte-Pelkum, V., & Behr, W. M. (2021). The competing effects of olivine and orthopyroxene cpo on seismic anisotropy. *Tectonophysics*, *814*, 228954. https://doi.org/https://doi.org/10.1016/j.tecto.2021.228954

Blackman, D. K., Orcutt, J. A., Forsyth, D. W., & Kendall, J.-M. (1993). Seismic anisotropy in the mantle beneath an oceanic spreading centre. *Nature*, *366*, 675–677.

Bodin, T., & Sambridge, M. (2009). Seismic tomography with the reversible jump algorithm. *Geophysical Journal International*, *178*, 1411–1436.

Bodmer, M., Toomey, D. R., Hooft, E. E., Nábělek, J., & Braunmiller, J. (2015). Seismic anisotropy beneath the juan de fuca plate system: Evidence for heterogeneous mantle flow. *Geology*, *43*, 1095–1098.

Bodmer, M., Toomey, D. R., VanderBeek, B., Hooft, E. E., & Byrnes, J. S. (2020). Body wave tomography of the cascadia subduction zone and juan de

fuca plate system: Identifying challenges and solutions for shore-crossing data. *Geochemistry, Geophysics, Geosystems*, *21*, e2020GC009316.

Browaeys, J. T., & Chevrot, S. (2004). Decomposition of the elastic tensor and geophysical applications. *Geophysical Journal International*, *159*, 667–678.

Buland, R., & Chapman, C. H. (1983). The computation of seismic travel times. *Bulletin of the Seismological Society of America*, *73*, 1271–1302.

Bunge, H.-P., & Grand, S. P. (2000). Mesozoic plate-motion history below the northeast pacific ocean from seismic images of the subducted farallon slab. *Nature*, *405*, 337–340.

Calvert, A. J., Ramachandran, K., Kao, H., & Fisher, M. A. (2006). Local thickening of the cascadia forearc crust and the origin of seismic reflectors in the uppermost mantle. *Tectonophysics*, *420*, 175–188. https://doi.org/https://doi.org/10.1016/j.tecto.2006.01.021

Cheng, C., Bodin, T., Tauzin, B., & Allen, R. M. (2017). Cascadia subduction slab heterogeneity revealed by three-dimensional receiver function kirchhoff migration. *Geophysical Research Letters*, *44*, 694–701.

Chevrot, S. (2000). Multichannel analysis of shear wave splitting. *Journal of Geophysical Research: Solid Earth*, *105*, 21579–21590.

Clennett, E. J., Sigloch, K., Mihalynuk, M. G., Seton, M., Henderson, M. A., Hosseini, K., Mohammadzaheri, A., Johnston, S. T., & Müller, R. D. (2020). A quantitative tomotectonic plate reconstruction of western north america and the eastern pacific basin. *Geochemistry, Geophysics, Geosystems*, *21*, e2020GC009117.

Crotwell, H. P., Owens, T. J., & Ritsema, J. (1999). The taup toolkit: Flexible seismic travel-time and ray-path utilities. *Seismological Research Letters*, *70*, 154–160.

Currie, C. A., Cassidy, J. F., Hyndman, R. D., & Bostock, M. G. (2004). Shear wave anisotropy beneath the cascadia subduction zone and western north american craton. *Geophysical Journal International*, *157*, 341–353.

Currie, C. A., & Yu, T.-C. (2023). Geodynamic studies of southwestern canada: Subduction zone processes and backarc mantle dynamics. *Canadian Journal of Earth Sciences*, *60*, 1283–1306.

DiPietro, J. A. (2018). *Geology and landscape evolution: General principles applied to the united states*. Elsevier.

Eakin, C. M., Obrebski, M., Allen, R. M., Boyarko, D. C., Brudzinski, M. R., & Porritt, R. (2010). Seismic anisotropy beneath cascadia and the mendocino

triple junction: Interaction of the subducting slab with mantle flow. *Earth and Planetary Science Letters*, *297*, 627–632.

English, J. M., & Johnston, S. T. (2004). The laramide orogeny: What were the driving forces? *International Geology Review*, *46*, 833–838.

Faccenda, M., & Capitanio, F. A. (2013). Seismic anisotropy around subduction zones: Insights from three-dimensional modeling of upper mantle deformation and sks splitting calculations. *Geochemistry, Geophysics, Geosystems*, *14*, 243–262.

Faccenda, M., Ferreira, A. M. G., Tisato, N., Lithgow-Bertelloni, C., Stixrude, L., & Pennacchioni, G. (2019). Extrinsic elastic anisotropy in a compositionally heterogeneous earth's mantle. *Journal of Geophysical Research: Solid Earth*, *124*, 1671–1687.

Faccenda, M., & VanderBeek, B. P. (2023). On constraining 3d seismic anisotropy in subduction, mid-ocean-ridge, and plume environments with teleseismic body wave data. *Journal of Geodynamics*, *158*, 102003.

Ford, M. T., Grunder, A. L., & Duncan, R. A. (2013). Bimodal volcanism of the high lava plains and northwestern basin and range of oregon: Distribution and tectonic implications of age-progressive rhyolites. *Geochemistry, Geophysics, Geosystems*, *14*, 2836–2857.

Fuston, S., & Wu, J. (2020). Raising the resurrection plate from an unfolded-slab plate tectonic reconstruction of northwestern north america since early cenozoic time. *GSA Bulletin*, *133*, 1128–1140. https://doi.org/10.1130/B35677.1

Gao, H., & Long, M. D. (2022). Tectonics and geodynamics of the cascadia subduction zone. *Elements: An International Magazine of Mineralogy, Geochemistry, and Petrology*, *18*, 226–231.

Gao, H., & Shen, Y. (2014). Upper mantle structure of the cascades from full-wave ambient noise tomography: Evidence for 3d mantle upwelling in the back-arc. *Earth and Planetary Science Letters*, *390*, 222–233.

Han, S., Carbotte, S. M., Canales, J. P., Nedimović, M. R., Carton, H., Gibson, J. C., & Horning, G. W. (2016). Seismic reflection imaging of the juan de fuca plate from ridge to trench: New constraints on the distribution of faulting and evolution of the crust prior to subduction. *Journal of Geophysical Research: Solid Earth*, *121*, 1849–1872.

Hawley, W. B., Allen, R. M., & Richards, M. A. (2016). Tomography reveals buoyant asthenosphere accumulating beneath the juan de fuca plate. *Science*, *353*, 1406–1408.

Hyndman, R. D., & Currie, C. A. (2011). Why is the north america cordillera high? hot backarcs, thermal isostasy, and mountain belts. *Geology*, *39*, 783–786. https://doi.org/10.1130/G31998.1

Ismat, Z., Putera, H., & Patzkowsky, S. (2022). Internal deformation of the gorda plate and its tectonic significance within the cascadia subduction zone. *Journal of Structural Geology*, *161*, 104643.

Itin, Y. (2018). Irreducible matrix resolution of the elasticity tensor for symmetry systems. *arXiv preprint arXiv:1812.03367*.

Karato, S.-i. (2024). Recent progress in the study of lattice-preferred orientation of olivine. *Journal of Geodynamics*, *161*, 102033. https://doi.org/https://doi.org/10.1016/j.jog.2024.102033

Karato, S.-i., Jung, H., Katayama, I., & Skemer, P. (2008). Geodynamic significance of seismic anisotropy of the upper mantle: New insights from laboratory studies. *Annu. Rev. Earth Planet. Sci.*, *36*, 59–95.

Kennett, B. L. N., Engdahl, E. R., & Buland, R. (1995). Constraints on seismic velocities in the earth from traveltimes. *Geophysical Journal International*, *122*, 108–124.

Liu, K. H., Elsheikh, A., Lemnifi, A., Purevsuren, U., Ray, M., Refayee, H., Yang, B. B., Yu, Y., & Gao, S. S. (2014). A uniform database of teleseismic shear wave splitting measurements for the western and central united states. *Geochemistry, Geophysics, Geosystems*, *15*, 2075–2085.

Löberich, E., Long, M. D., Wagner, L. S., Qorbani, E., & Bokelmann, G. (2021). Constraints on olivine deformation from sks shear-wave splitting beneath the southern cascadia subduction zone back-arc. *Geochemistry, Geophysics, Geosystems*, *22*, e2021GC010091.

Long, M. D. (2016). The cascadia paradox: Mantle flow and slab fragmentation in the cascadia subduction system. *Journal of Geodynamics*, *102*, 151–170.

Long, M. D., & Becker, T. W. (2010). Mantle dynamics and seismic anisotropy. *Earth and Planetary Science Letters*, *297*, 341–354. https://doi.org/https://doi.org/10.1016/j.epsl.2010.06.036

Mainprice, D., Tommasi, A., Couvy, H., Cordier, P., & Frost, D. J. (2005). Pressure sensitivity of olivine slip systems and seismic anisotropy of earth's upper mantle. *Nature*, *433*, 731–733.

Martin-Short, R., Allen, R. M., Bastow, I. D., Totten, E., & Richards, M. A. (2015). Mantle flow geometry from ridge to trench beneath the gorda–juan de fuca plate system. *Nature Geoscience*, *8*, 965–968.

Mosher, S. G., Audet, P., & L'Heureux, I. (2014). Seismic evidence for rotating mantle flow around subducting slab edge associated with oceanic microplate capture. *Geophysical Research Letters*, *41*, 4548–4553.

Mullen, E. K., & Weis, D. (2015). Evidence for trench-parallel mantle flow in the northern cascade arc from basalt geochemistry. *Earth and Planetary Science Letters*, *414*, 100–107.

Munzarová, H., Plomerová, J., & Kissling, E. (2018). Novel anisotropic teleseismic body-wave tomography code anitomo to illuminate heterogeneous anisotropic upper mantle: Part i — theory and inversion tuning with realistic synthetic data. *Geophysical Journal International*, *215*, 524–545. https://doi.org/10.1093/gji/ggy296

Obrebski, M., Allen, R. M., Pollitz, F., & Hung, S.-H. (2011). Lithosphere–asthenosphere interaction beneath the western united states from the joint inversion of body-wave traveltimes and surface-wave phase velocities. *Geophysical Journal International*, *185*, 1003–1021.

Obrebski, M., Allen, R. M., Xue, M., & Hung, S.-H. (2010). Slab-plume interaction beneath the pacific northwest. *Geophysical Research Letters*, *37*.

Paige, C. C., & Saunders, M. A. (1982). Lsqr: An algorithm for sparse linear equations and sparse least squares. *ACM Transactions on Mathematical Software (TOMS)*, *8*, 43–71.

Piccolo, G. D., VanderBeek, B. P., Faccenda, M., Morelli, A., & Byrnes, J. S. (2024). Imaging upper-mantle anisotropy with transdimensional bayesian monte carlo sampling. *Bulletin of the Seismological Society of America*, *114*, 1214–1226.

Riddihough, R. P., Beck, M. E., Chase, R. L., Davis, E. E., Hyndman, R. D., Johnson, S. H., & Rogers, G. C. (1983). Geodynamics of the juan de fuca plate. *Geodynamics of the Eastern Pacific Region, Caribbean and Scotia Arcs*, *9*, 5–21.

Rowan, C. J., & Rowley, D. B. (2014). Spreading behaviour of the pacific-farallon ridge system since 83 ma. *Geophysical Journal International*, *197*, 1273–1283.

Russo, R. M. (2009). Subducted oceanic asthenosphere and upper mantle flow beneath the juan de fuca slab. *Lithosphere*, *1*, 195–205.

Schellart, W. P., Stegman, D. R., Farrington, R. J., Freeman, J., & Moresi, L. (2010). Cenozoic tectonics of western north america controlled by evolving width of farallon slab. *Science*, *329*, 316–319.

Schmandt, B., & Humphreys, E. (2010). Complex subduction and small-scale convection revealed by body-wave tomography of the western united states upper mantle. *Earth and Planetary Science Letters*, *297*, 435–445.

Sella, G. F., Dixon, T. H., & Mao, A. (2002). Revel: A model for recent plate velocities from space geodesy. *Journal of Geophysical Research: Solid Earth*, *107*, ETG–11.

Seton, M., Müller, R. D., Zahirovic, S., Gaina, C., Torsvik, T., Shephard, G., Talsma, A., Gurnis, M., Turner, M., & Maus, S. (2012). Global continental and ocean basin reconstructions since 200 ma. *Earth-Science Reviews*, *113*, 212–270.

Sieminski, A., Liu, Q., Trampert, J., & Tromp, J. (2007). Finite-frequency sensitivity of body waves to anisotropy based upon adjoint methods. *Geophysical Journal International*, *171*, 368–389.

Silver, P. G., & Chan, W. W. (1991). Shear wave splitting and subcontinental mantle deformation. *Journal of Geophysical Research: Solid Earth*, *96*, 16429–16454.

Storchak, D. A., Schweitzer, J., & Bormann, P. (2003). The iaspei standard seismic phase list. *Seismological Research Letters*, *74*, 761–772. https://doi.org/10.1785/gssrl.74.6.761

Tasaka, M., Zimmerman, M. E., Kohlstedt, D. L., Stünitz, H., & Heilbronner, R. (2017). Rheological weakening of olivine+ orthopyroxene aggregates due to phase mixing: Part 2. microstructural development. *Journal of Geophysical Research: Solid Earth*, *122*, 7597–7612.

Tauzin, B., Bodin, T., Debayle, E., Perrillat, J.-P., & Reynard, B. (2016). Multi-mode conversion imaging of the subducted gorda and juan de fuca plates below the north american continent. *Earth and Planetary Science Letters*, *440*, 135–146.

Team, T. M. S. (1998). Imaging the deep seismic structure beneath a mid-ocean ridge: The melt experiment. *Science*, *280*, 1215–1218.

Thomsen, L. (1986). Weak elastic anisotropy. *Geophysics*, *51*, 1954–1966.

Turcotte, D. L., & Schubert, G. (2002). *Geodynamics*. Cambridge university press.

VanderBeek, B. P., Bue, R. L., Rappisi, F., & Faccenda, M. (2023). Imaging upper mantle anisotropy with traveltime and splitting intensity observations from teleseismic shear waves: Insights from tomographic reconstructions of subduction simulations. *Geophysical Journal International*, *235*, 2640–2670.

VanderBeek, B. P., & Faccenda, M. (2021). Imaging upper mantle anisotropy with teleseismic p-wave delays: Insights from tomographic reconstructions of subduction simulations. *Geophysical Journal International*, *225*, 2097–2119.

VanderBeek, B. P., & Toomey, D. R. (2017). Shallow mantle anisotropy beneath the juan de fuca plate. *Geophysical Research Letters*, *44*, 11–382.

Wang, X., Chen, L., Wang, K., Chen, Q.-F., Zhan, Z., & Yang, J. (2024). Seismic evidence for melt-rich lithosphere-asthenosphere boundary beneath young slab at cascadia. *Nature Communications*, *15*, 3504.

Warren, J. M., Hirth, G., & Kelemen, P. B. (2008). Evolution of olivine lattice preferred orientation during simple shear in the mantle. *Earth and Planetary Science Letters*, *272*, 501–512. https://doi.org/https://doi.org/10.1016/j.epsl.2008.03.063

West, J. D., Fouch, M. J., Roth, J. B., & Elkins-Tanton, L. T. (2009). Vertical mantle flow associated with a lithospheric drip beneath the great basin. *Nature Geoscience*, *2*, 439–444.

Wilson, D. S. (1988). Tectonic history of the juan de fuca ridge over the last 40 million years. *Journal of Geophysical Research: Solid Earth*, *93*, 11863–11876.

Wu, M., Wang, H., Zhang, S., & Ritzwoller, M. H. (2023). Plate age and uppermost mantle structure across the juan de fuca and gorda plates. *Journal of Geophysical Research: Solid Earth*, *128*, e2023JB026494.

Zandt, G., & Humphreys, E. (2008). Toroidal mantle flow through the western us slab window. *Geology*, *36*, 295–298.

Zhao, D., & Hua, Y. (2021). Anisotropic tomography of the cascadia subduction zone. *Physics of the Earth and Planetary Interiors*, *318*, 106767.

Zhou, Q., Hu, J., Liu, L., Chaparro, T., Stegman, D. R., & Faccenda, M. (2018). Western us seismic anisotropy revealing complex mantle dynamics. *Earth and Planetary Science Letters*, *500*, 156–167.

Acknowledgments

I would like to thank Prof. Manuele Faccenda and Dott. Brandon Vanderbeek for there continued help and support throughout this project.

7

Appendix

Table 7.1: List of Seismic Networks, Operating Institutions, and Dates from which data was used in this study.

Seismic Network	Operating institutions	Operational Dates
7D	Cascadia initiative Community experiment	01/01/2011 - 31/12/2017
BK	Berkley digital seismic network	18/11/2016 - 27/06/2024
CC	Cascadia Chain Volcano Monitoring	01/01/2001 - Present
CN	Canadian National Seismographic Network	01/01/1980 - Present
GS	US Geological Survey Networks	01/01/1980 - Present
HW	Hanford Washington Seismic Netwrok	01/01/1980 - Present
IM	International Miscellaneous Stations	01/01/1980 - Present
IU	Global Seismograph Network	24/01/2000 - Present
IW	Intermountain West Seismic Network	01/01/2003 - Present
LB	Leo Brady Network	23/06/1994 - Present
NN	Nevada Seismic Network/ Western Great Basin	01/08/1972 - Present

NV	Neptune Canada	01/01/2009 - Present
OO	Ocean Observatories Initiative	01/01/2003 - Present
TA	USArray Transportable Array (NSF EarthScope Project)	19/07/2004 - 30/09/2016
UO	Pacific Northwest Seismic Network - University of Oregon	01/02/1994 - Present
US	United States National Seismic Network	15/06/1992 - Present
UW	Pacific Northwest Regional Seismic Network	09/06/1992 - Present
X9	Plate Boundary Evolution and Physics at an Oceanic Transform Fault System	01/01/2012 - 31/12/2013
XD	Collaborative Research: Illuminating the architecture of the greater Mount St. Helens magmatic systems from slab to surface	01/01/2014 - 31/12/2016
XT	Deformation and Magmatic Modification of a Steep Continental Margin, Western ID-Eastern Oregon	01/01/2011 - 31/12/2013
YU	Northern California Delta	01/01/2006 - 31/12/2014
YX	Flexarray 3D Passive Seismic Imaging of Core-Complex Extension in the Ruby Range Nevada	01/01/2010 - 31/12/2012
Z5	Seismicity, Structure and Dynamics of the Gorda Deformation Zone	01/01/2013 - 31/12/2015
ZH	Monitoring seismicity associated with a possible asperity on the Cascadia megathrust	01/01/2011 - 31/12/2012

ZZ	Collaborative Research: Imaging the Cascadia subduction zone - a ship-to-shore opportunity	01/01/2012 - 31/12/2012